

Antenna-coupled integrated millimeterwave modulators and resonant electro-optic frequency combs

Aleksei Gaier^{1, 2}, Karen Mamian¹, Shima Rajabali^{3, 4}, Yazan Lampert^{1, 2}, Jiawen Liu^{1, 2}, Leticia Magalhaes³, Amirhassan Shams-Ansari⁵, Marko Lončar³, and Ileana-Cristina Benea-Chelmus^{1,2}

¹*Hybrid Photonics Laboratory, École Polytechnique Fédérale de Lausanne (EPFL), CH-1015, Switzerland*

²*Center for Quantum Science and Engineering (QSE), CH-1015, Switzerland*

³*Harvard John A. Paulson School of Engineering and Applied Sciences, Harvard University, Cambridge, MA, USA*

⁴*Department of Quantum and Computer Engineering, Delft University of Technology, Netherlands*

⁵*DRS Daylight Solutions, 16465 Via Esprillo, CA, USA*

May 8, 2025

Abstract

The rapid growth of global data traffic is accelerating the need for ultra-broadband communication technologies, particularly in inter-data center links, cloud infrastructure, and emerging 6G wireless systems. Applications such as optical computing and quantum information processing further demand fast, scalable ways to interface optical and electronic signals. Integrated electro-optic modulators offer a compact and efficient solution, but extending their operation into the millimeterwave (mmWave) and terahertz regimes while providing wide operational bandwidths and compatibility with wireless mmWave signals is difficult. Key challenges include high transmission line losses and bulky electrical packaging, limiting the performance and scalability of these systems.

Here, we demonstrate a wireless and wideband electro-optic modulation architecture that directly interfaces wireless mmWave signals with optical ones, eliminating the need for impedance-matched mmWave probes and cables. By integrating an on-chip antenna directly with a co-designed traveling-wave transmission line on thin-film lithium niobate, we achieve spectrally flat phase modulation across the WR9.0 (82–125 GHz) and WR2.8 (240–380 GHz) bands. The wideband nature of our modulator enables the device to function as a high-speed mmWave detector. By modulating the mmWave carrier at frequencies up to 6 GHz, we demonstrate the device’s flat and wide detection bandwidth—critical for 6G communication and high-speed mmWave sensing. Beyond traveling-wave detection, our wireless platform enables resonant electro-optic frequency comb generation with mode spacing of 123.2 GHz and 307.9 GHz. Extracted single-photon electro-optic coupling rates of $g_{eo} = 2\pi \times 10.61$ kHz and 25.99 kHz, at 123.2 and 307.9 GHz, respectively, demonstrate favorable scaling with mmWave frequency. These results establish a new class of broadband, wireless electro-optic devices for high-speed modulation, detection, and frequency comb generation, with promising applications in communications, sensing, and quantum technologies.

1 Introduction

The rapid expansion of cloud services, AI workloads, and global data exchange has led to an unprecedented surge in data traffic, placing stringent demands on the underlying communication infrastructure [1]. Exploiting under-utilized

frequency bands such as the mmWave (30-300 GHz) and the terahertz (300 GHz - 10 THz) offers a promising path to meet the demand for this ever-increasing growth [2]. These bands provide access to much larger available bandwidths than traditional microwave frequencies while offering improved robustness to atmospheric turbulence compared to free-space optical communications at telecom frequencies. However, all-electronic transmitters, receivers and mixers needed to establish a mmWave/terahertz communication link, typically based on high-frequency electronic devices such as high-electron-mobility transistors [3] or Schottky barrier diodes [4], face fundamental challenges. In particular, the signal integrity and the bandwidth of these systems are limited due to technical issues. For example, a typical way to generate high-frequency signals is to implement the frequency extenders [4]. However, these components generate several harmonics of the fundamental frequency, and the insufficient suppression of undesired harmonics compromises the purity of the generated signal [5]. Similarly, the bandwidth of the intermediate frequencies (IF) of commercial all-electronic mixers is about a few tens of gigahertz, limiting the data modulation (demodulation) speed at the sender (receiver) end [6]. Moreover, high power consumption for signal generation and amplification, and susceptibility to electrostatic discharge (ESD) impose further constraints on all-electronic systems [7].

To address these limitations while achieving large operating bandwidth, photonic technologies have emerged as a powerful alternative [8, 9]. By enabling the interaction between microwave signals and optical carriers, photonics offers access to significantly broader bandwidths, reduced long-distance losses, and multiplexing capabilities. This field, often referred to as radio-frequency (RF) photonics, has already demonstrated transformative potential in high-speed communications [10] and advanced sensing systems [11]. A key component in current communication networks that overcomes these problems at the receiver end is an integrated electro-optic modulator, which converts microwave signals to the optical domain within a compact and power-efficient chip. Of particular interest for next generation communications systems are wireless modulators which are designed to directly capture free-space signals and encode them onto optical carriers [2]. By providing a direct interface between the wireless signals used in communications systems such as 5G, with optical data transmission infrastructure, these modulators enable high-capacity links between wireless access points and long-haul fiber networks.

To further meet the demands of next-generation technologies such as the emerging 6G networks, there is a growing interest in extending the operation of electro-optic modulators from traditional microwave frequencies into the millimeter-wave (mmWave) and terahertz (THz) regimes [2]. Among various mechanisms explored for phase and intensity modulation, second-order ($\chi^{(2)}$) nonlinearities stand out due to their intrinsically fast electronic response, enabling modulation bandwidths that far exceed the limitations of carrier-based modulators. High-speed modulation in mmWave and THz spectral bands would not only benefit optical communication but also enable critical advances in quantum optics [12, 13, 14], quantum transduction between optical and microwave domains [15], mmWave radar and ranging systems [16, 11], and quantum computing architectures [17, 18, 19].

Achieving efficient light modulation at mmWave and THz frequencies, while maintaining compact, integrated, and low-loss device architectures, remains a key technological challenge. This has driven extensive research across various material platforms [20]. Material platforms under investigation include lithium niobate [21, 22, 23, 10], hybrid silicon nitride–lithium niobate [24, 25], hybrid silicon-organic modulators [26, 27, 28, 9], aluminum nitride [29], barium titanate [30] and lithium tantalate [8].

When it comes to the platform selection for mm-Wave and THz, two properties must be considered, namely the THz loss, and the broadband nonlinearity of the material. Among these, in terms of THz loss aluminum nitride stands out due the high frequency of its optical phonon [31]. However, it suffers from relatively low electro-optic coefficients ($r_{33} = -0.59$ pm/V) [29]. In contrast, barium titanate has extremely high Pockels coefficients ($r_{42} = 500$ pm/V). How-

ever in addition to large THz loss [32], its nonlinearity rolls-off rapidly at modulation frequencies beyond 80 GHz [30]. Organic materials have low terahertz loss and achieve the record-breaking modulation bandwidths [9]. However, it is important to note that organics suffer from relatively high optical absorption and do not yet form a stand-alone photonic platform, necessitating integration e.g. with silicon-on-insulator [33, 34]. Thin film lithium niobate (TFLN) offers both low optical loss, moderate nonlinearities and high-power stability. Recently, TFLN has been used for both broadband terahertz generation [35, 36], and terahertz detection and beam profiling at 500 GHz [37] as early demonstrations of hybrid THz-photonics devices.

A critical but relatively underexplored challenge in developing of mmWave electro-optic modulators is efficiently delivering the mmWave signal on to the chip. Currently, most demonstrations rely on probe-based coupling methods, which become increasingly fragile, expensive, and difficult to scale at frequencies above a few tens of gigahertz. These methods experience significant attenuation of high-frequency signals due to decreasing skin depth (scaling with $\propto \sqrt{f_{mmW}}$ [38, 39]). Both the electrical circuit delivering the mmWave signals to the photonic chip and RF circuit on the chip contribute to this loss. Another complication arises from increased radiative losses which scales as $\propto w^2 f_{mmW}^3$ [39, 40], with w being the distance between ground and signal electrodes. This scaling leads to elevated cross-talk at higher frequencies. Additionally, impedance matching between the coaxial cables, the RF probes, and the on-chip transmission line (typically 50 Ω) presents a significant challenge in mmWave and THz regimes. We would note that the current mmWave delivery technology relies on rectangular waveguides to mitigate radiative and metallic loss. However, these waveguides are bulky and lack the necessary flexibility for practical application and integration.

These challenges highlight the need for developing practical and low-loss techniques to enhance the efficiency of electro-optic modulation across the entire signal path. Transitioning from wired to wireless approaches offers a promising solution by transmitting millimeterwave signals through free space, thereby avoiding ohmic losses, and directly coupling them into the chip via large aperture, eliminating the need for complex interfaces. Previous demonstrations [26, 11, 41, 42] have been restricted to a relatively narrow operational bandwidth.

In this work, we propose a wireless and wideband mmWave and terahertz electro-optic modulator on thin film lithium niobate platform that operates across the WR9.0 (82-125 GHz) and WR2.8 (240-380 GHz) bands (Fig. 1 a). Our device implements an on-chip antenna coupling free-space terahertz radiation to an on-chip transmission line eliminating the need for complex and fragile terahertz signal delivery components. To ensure the broadband operation of this device, the index of the mm-Wave traveling across the transmission line is engineered to match the group index of the optical signal enabling velocity matching over a wide frequency range. Furthermore, we integrate a hyper-hemispherical silicon lens on the backside of our TFLN chip (aligned with the on-chip antenna) to improve the coupling efficiency of the incoming mmWave/terahertz signal (Fig. 1 b). Upon being illuminated by the external mmWave source, the antenna becomes a mmWave signal generator with a voltage amplitude V_a and characteristic impedance Z_a that can be tailored through design. This flexibility significantly simplifies the co-design of the transmission line to minimize optical and mmWave losses while maximizing the modulation efficiency. We note that such miniaturized mmWave devices are incompatible with conventional characterization techniques, necessitating innovative approaches to extract the mmWave transmission line parameters. To address this we develop a photonics-based characterization technique showing excellent agreement between theory and experiment. Our method is a step towards verification of thin films properties against their bulk counterparts at mmWave frequencies.

Leveraging our flat frequency response we realize a miniaturized high-speed terahertz detector (Fig. 1 c). In contrast to the state-of-the-art terahertz detectors that rely on pyroelectric effect limiting their speed to a few kHz, our device operates 6-orders of magnitude faster, reaching several gigahertz range. This dramatic improvement

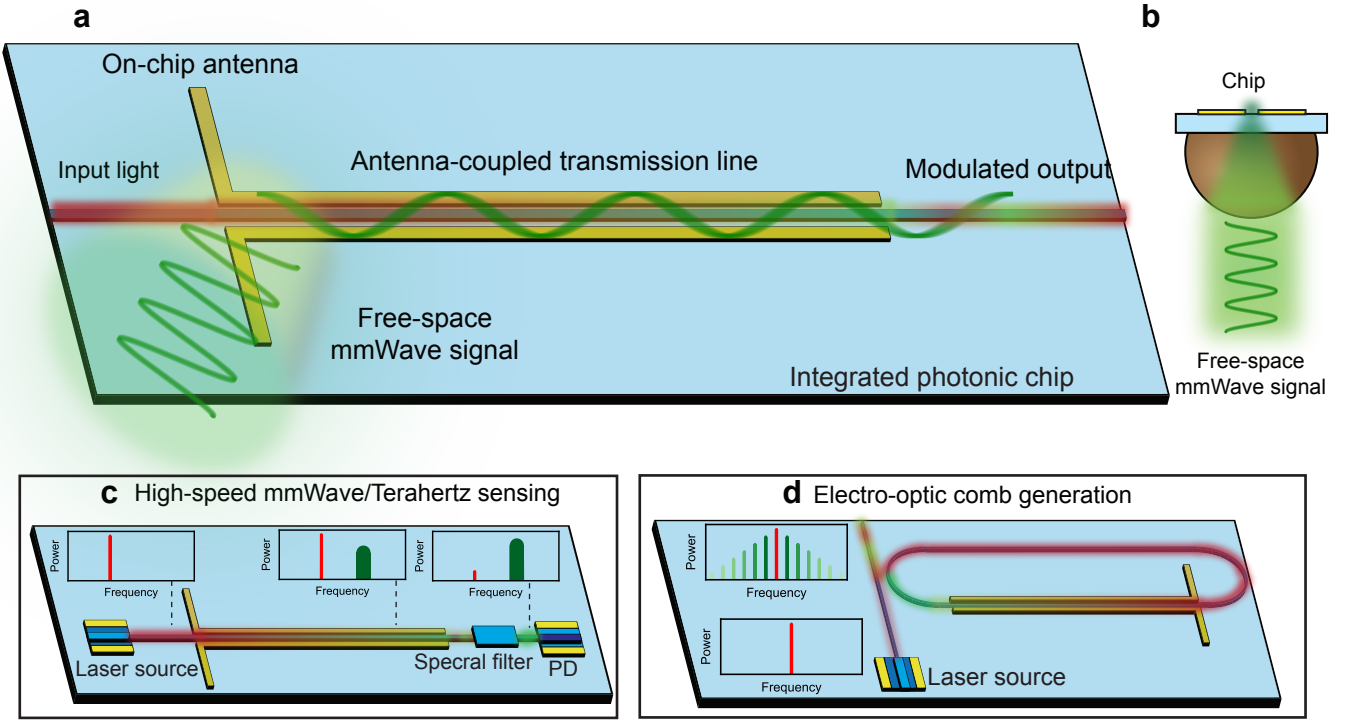


Fig. 1: Wideband wireless electro-optic (EO) modulator in TFLN and its applications in high-speed sensing and frequency comb formation. (a) Conceptual sketch of a wireless electro-optic (EO) modulator, where a free-space mmWave signal is captured by an on-chip antenna and coupled to a transmission line. This transmission line runs adjacent to an optical waveguide fabricated in thin-film lithium niobate (TFLN), enabling phase modulation of the guided light via the electro-optic effect. (b) Illustration of the wireless signal delivery scheme, where an incoming mmWave or terahertz beam is focused onto an on-chip antenna using a hyper-hemispherical silicon lens to maximize coupling efficiency. (c) Schematic of a high-speed free-space radiation sensor based on the wireless EO modulator. A laser pumps the optical waveguide, and incident mmWave or terahertz radiation induces phase modulation in the optical path, generating an optical sideband in the frequency domain. Then the carrier frequency is filtered, and then the sideband is detected by a photodiode (PD). (d) Diagram of an EO comb generator architecture utilizing the wireless EO modulator, where the incoming wireless signal induces a modulated optical spectrum suitable for applications in spectroscopy and communication.

stems from its operation based on the ultra-fast electro-optic effect with its detection speed currently limited by the modulation bandwidth of the incoming signal. Finally, we leverage the low-loss nature of TFLN platform and place our phase modulator in a racetrack cavity (Fig. 1 d). This enhances the effective path length over which the optical signal interacts with the mmWave, and results in a cascaded sideband generation. Using this, we realize a proof-of-principle electro-optic frequency comb source with adjustable mmWave line spacings of 123 GHz and 308 GHz.

Altogether, our work lays the theoretical and experimental foundation for designing wireless terahertz modulators with smaller footprints, enabling scalability, broad bandwidths, and discusses strategies to achieve higher efficiencies through resonant nonlinear effects.

2 Results

Antenna-transmission line co-design rules

Similar to conventional modulators, for our wired modulator we need to ensure that the mmWave signal on-chip is maximized, while optimizing the interaction with the optical carrier. The antenna design dictates the amount of

power which is collected from free space and delivered to the transmission line, while the transmission line design would impact the modulation efficiency between the optical probe and the mmWave signal. Our theoretical model provides the following design guidelines:

i) **The transmission line:** Our wireless modulator performance metrics requires the transmission line to maintain a coherence length (L_{coh}) larger than the device length L_{TL} , minimize mmWave propagation loss α_{Ω} , maximize spatial overlap Γ_{eo} between the optical and mmWave modes, and achieve strong mmWave mode confinement by reducing the mode cross-section S_{Ω} . However, unlike conventional modulators, our wireless modulator does not require the impedance matching between the characteristic impedance of the transmission line Z_{TL} and 50 ohms cables and delivery circuitry.

ii) **The antenna:** The antenna must be optimized to collect the maximum amount of the incident mmWave from the free space E_{inc} . Upon the incidence, the antenna generates a voltage wave V_a across its gap. The goal is to maximize the frequency-dependent inverse antenna factor ($IAF = \frac{V_a}{E_{inc}}$). Additionally, we need to ensure impedance matching between the antenna and the transmission line ($Z_a = Z_{TL}$) to accomplish maximum delivery of the collected wave to the transmission line.

Wideband mmWave wireless modulator

To meet the design rules, we optimize two critical transmission line parameters, namely, the electrode gap ($w = 3.3 \mu\text{m}$), and the optical waveguide width ($w_{wg} = 1.5 \mu\text{m}$) to achieve impedance matching, minimize the metal-related absorption, and maximize the coherence length (full design spec in the Supplementary Information section 1). We achieve an optical loss of 1 dB/mm, mode overlap factor of $\Gamma_{eo} = 0.54$, and coherence length of $L_{coh} = 5 \text{ mm}$ with the aforementioned values for the waveguide width and electrode gap. We note that the measured optical loss is higher than state-of-the-art values [43], however we chose this narrower gap to achieve a small mode area and hence improve the modulation, highlighting the importance of balancing these parameters rather than minimizing the loss alone.

On the antenna's side, we opt for a dipolar design as opposed to bow-tie antennas since its resonant behavior will boost the IAF . However, this comes at the cost of a frequency-dependent impedance Z_a which complicates the impedance matching with the transmission line leading to reflection of the incident mmWave signal at the transmission line interface (see details in the Supplementary Information section 5). Our simulations confirm that an antenna design with a length of $400 \mu\text{m}$ gives high values of IAF at frequency range 50-500 GHz and a moderate reflection coefficient $r_a = 0.6$. Further details in Supplementary Information section 2.1 and 8.

The devices are fabricated in an x-cut thin film lithium niobate substrate similar to our previous work [36, 37]. The transmission lines are $L_{TL} = 2 \text{ mm}$ long which is limited by mmWave loss. We illuminate our devices with free-space mmWave radiation from a frequency extender system equipped with horn antennas emitting a Gaussian mmWave beam (Fig. 2 a). We investigate two scenarios: configuration A - short range ($< 10 \text{ cm}$) to simulate signal delivery in a constrained space such as inside a cryostat for quantum experiments and configuration B - medium range ($10 - 100 \text{ cm}$) for applications in open spaces, such as 6G communications (shown in Fig. 2 b). Details on the fabrication and the experimental setup in the methods and Supplementary Information section 1.

First, we butt-couple 1550 nm continuous wave light to the chip through its edge (9 dB/facet). The polarization of the light is aligned with the z-axis of lithium niobate (TE). To ensure the maximum modulation efficiency, and benefiting from the largest component of the nonlinear susceptibility tensor $\chi_{333}^{(2)}$, the antenna collects the free-space radiation into the plane of TFLN (z-axis), and couples it to the transmission line generating an electric field parallel

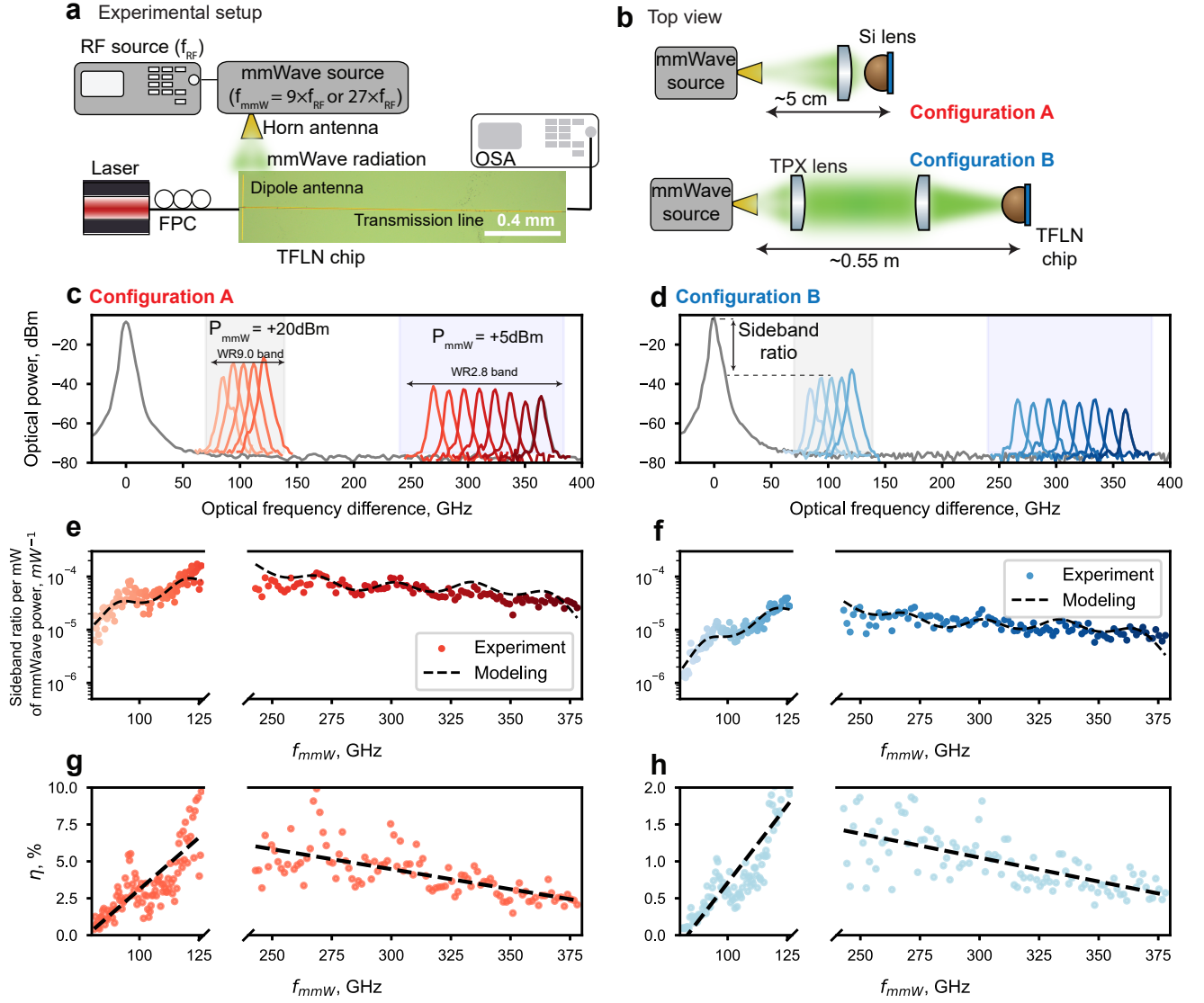


Fig. 2: Experimental results demonstrating the performance of wireless TFLN electro-optic modulators. (a) Schematic of the setup: an RF source generating 10 dBm of continuous-wave microwave signal at frequencies between 9–14 GHz drives a frequency chain multiplier (mmWave source) with a multiplication factor of 9 (WR9.0 band) or 27 (WR2.8 band). The resulting mmWave signal is emitted into free space via a horn antenna and illuminates the photonic chip, which is simultaneously pumped by 1550 nm light from a laser. The output spectra are recorded using an optical spectrum analyzer (OSA). FPC – fiber polarization controller. The plot also includes a photograph of the measured device, which shows a TFLN rib waveguide along which we pattern the antenna-coupled transmission line of length L_{TL} . (b) Top-view sketch of the experimental setup: Configuration A (short range) investigates our modulators upon short-distance illumination. The mmWave beam is focused onto the chip using a single TPX (polymethylpentene) lens, with a total distance of 5 cm from the horn antenna to the chip. Configuration B (medium range) corresponds to a setup with an increased distance of 0.55 m, where the beam is first collimated by a TPX lens and then focused by a second TPX lens. In both cases we attach a hyper-hemispherical silicon (Si) lens to the back-side of the TFLN chip. (c) Measured optical spectra for various mmWave frequencies in Configuration A, offset from the optical carrier frequency. (d) Measured optical spectra for various mmWave frequencies in Configuration B, offset from the optical carrier frequency. (e) Sideband ratio per mW of incident mmWave power as a function of frequency in Configuration A. (f) Sideband ratio per mW of incident mmWave power as a function of frequency in Configuration B. (g) Coupling efficiency (η) as a function of frequency for Configuration A, calculated from Eq.1, with a linear fit shown as a dashed line. (h) Coupling efficiency (η) as a function of frequency for Configuration B, with linear fit shown as a dashed line.

to the polarization optical field. In the frequency domain, the phase modulation (three-wave mixing) between the optical carrier and the mm-Wave generates two optical sidebands. We quantify the modulator’s efficiency with the

side band ratio (SBR) at a given mmWave power incident onto the chip $P_{mmW}^{free-space}$, which is the ratio between the optical power in each sideband and the power of the optical signal. SBR depends on the experimental parameters as follows:

$$SBR = \frac{(\chi^{(2)} \cdot \omega_o)^2 \cdot \Gamma_{eo}^2 \cdot L_{TL}^2 \cdot PM^2}{2 \cdot n_o^2 \cdot n_\Omega \cdot c_0^3 \cdot \varepsilon_0 \cdot S_\Omega} \cdot \eta P_{mmW}^{free-space} \quad (1)$$

where $\chi^{(2)} = \chi_{333}^{(2)}$, ω_o is the optical angular frequency, n_o is the effective refractive index of the optical mode, c_0 is the speed of light in vacuum and ε_0 is the vacuum permittivity. $PM = \left| \frac{e^{i\Delta\tilde{k}L_{TL}} - 1}{\Delta\tilde{k}L_{TL}} \right|$ is the phase-matching function quantifying any propagation phase acquired between the interacting fields along the transmission line's length $\Delta\tilde{k} = \frac{2\pi f_{mmW}}{c_0}(n_\Omega - n_g) + i\frac{\alpha_\Omega}{2}$, η is the coupling efficiency of mmWave power into the transmission line being proportional to the square of IAF, and $P_{mmW}^{free-space}$ is the power of the mmWave beam in free-space. Using these definitions, the corresponding on-chip power is $P_{mmW}^{on-chip} = \eta \cdot P_{mmW}^{free-space}$ (complete derivation in Supplementary Information section 2).

Our mmWave source provides 100 mW in the WR9.0 frequency range (82-125 GHz) and 5 mW in the WR2.8 frequency range (240-380 GHz) through a horn antenna which is coupled into the chip using a backside mounted silicon lens. The modulated optical signal is collected using a lensed fiber, and then visualized on an optical spectrum analyzer (Fig. 2 a-b, details in methods). Our wireless electro-optic modulators support efficient formation of sidebands across the entire incident mmWave range (Fig. 2 c-d). To gain quantitative insight into the efficiency of our broadband modulators and eliminate the effect of the variation in mmWave power from the source, we analyze the frequency-dependent efficiency of the modulator by reporting the sideband ratio per unit of milliwatt incident mmWave power (Fig. 2 e-f). In both configurations the antenna supports a spectrally flat sideband ratio across both bands. We extract values of $10^{-4}/\text{mW}$ and $3 \cdot 10^{-5}/\text{mW}$ for configuration A and configuration B, respectively. Using Eq. 1 we can estimate the amount of mmWave power coupled from free-space to the chip to be 1-8% across the WR9.0 band and 2-6% across the WR2.8 band, respectively (Fig. 2 g-h). The linear frequency dependence of these values is related to the frequency-dependent beam waist of the Gaussian mmWave beam generated by the horn antenna. We calculate a half-wave voltage-length product $V_\pi \cdot L_{TL} = \sqrt{2Z_{TL} \frac{P_{mmW}^{on-chip}}{SBR}} \cdot L_{TL}$ of 3.4 V·cm in WR9.0 and 3.65 V·cm at WR2.8 band, comparable to previous studies using wired mmWave electro-optic modulators [8].

Photonics-enabled characterization of mmWave transmission lines

The performance of our wireless modulators strongly depends on their mmWave loss, impedance and the transmission line's refractive index. At RF frequencies, these properties are routinely measured by performing a scattering matrix analysis using a vector network analyzer. For optimization purposes, it's essential to measure these values for our devices, but such instruments are expensive in the mmWaves, and their calibration requires a wired signal delivery.

We propose a photonics-enabled technique to extract the transmission line's parameters. Our method involves performing two experiments, as shown in Fig. 3 a and b. The direction of propagation of the optical signal is reversed between the two experiments, enabling interaction with the mmWave signal in either an optics-forward or an optics-backward configuration. In both cases, the mmWave travels forward along the transmission line, gets reflected at its end, and the returns. With phase-matching and sufficient single-pass mmWave losses (achieved by using long transmission lines), the mmWave signal is attenuated during its forward propagation. This makes the modulation more efficient in the optics-forward configuration compared to the optics-backward configuration where the added attenuation of the mmWave signal during forward propagation leads to a smaller side-band ratio, see Fig. 3 c for a transmission line length of $L_{TL} = 0.5$ mm. In addition, for short transmission line lengths L_{TL} , phase-matching

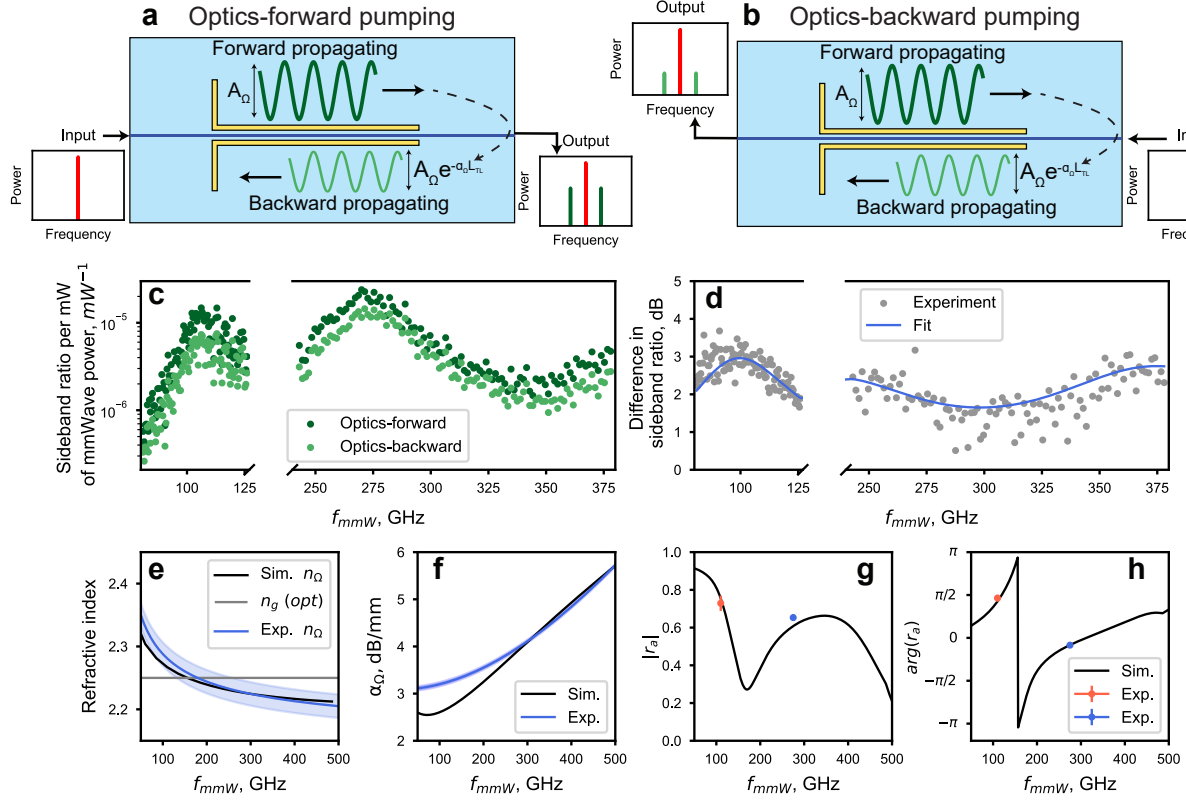


Fig. 3: Photonics-enabled characterization of loss and refractive index of mmWave transmission lines.

(a) Sketch of the experimental setup for the optics-forward pumping scheme. The optical signal is coupled from the left to the chip. The mmWave signal couples through the antenna to the transmission line, and has an amplitude A_Ω . It hence co-propagates with the optical signal in forward direction. As the mmWave signal propagates along the transmission line, it gets attenuated due to losses α_Ω . After reaching the end of the transmission line, the mmWave signal is reflected with approximately unity efficiency. The amplitude of the back-reflected wave is then $A_\Omega e^{-\alpha_\Omega L_{TL}}$. This counter-propagating mmWave signal also interacts with the optical signal, however with reduced efficiency since counter-propagating. Overall, the two processes (co- and counter-propagating optical and mmWave signals) lead to the formation of sidebands in the optical domain (shown as dark green lines in the output spectra). (b) Sketch of the experimental setup for the optics-backward pumping scheme. In this case the direction of propagation of the optical signal is swapped compared to the optics-forward scheme. The optical signal interacts with the forward-propagating mmWave signal in a counter-propagating configuration, whereas it interacts with the reflected mmWave signal in co-propagating configuration. For long transmission lines, the co-propagating configuration is better phase-matched, which results in weaker sidebands (shown as light green lines in the output spectra) since the back-reflected mmWave signal is attenuated due to mmWave loss. (c) Normalized sideband ratio for the optics-forward (dark green) and optics-backward (light green) configurations. We observe a lower sideband ratio for the optics-backward configuration, which allows estimating the transmission line losses α_Ω . There is also a clear frequency dependency, enabling the extraction of the antenna's reflection coefficient r_a , see text. (d) Ratio of optics-forward to optics-backward sideband ratios, shown in dB (gray points), along with the fitted curve (blue). The clear frequency dependency facilitates extracting the refractive index of the mmWave mode propagating along the transmission line, see text. (e) Comparison between simulated and fitted values of the refractive indices. (f) Comparison between simulated and fitted values of the mmWave losses. (g) Comparison between simulated and fitted absolute values of the antenna-transmission line reflection coefficient r_a . (h) Comparison between the simulated and fitted phase of the reflection coefficient.

occurs for both co-propagating and counter-propagating mmWave and optical signals, and the total modulation is a sum of these two contributions. This interference introduces the sinusoidal modulation in the ratio of the sideband-ratio Fig. 3 c. Relating the sideband ratios of these two measurements (shown in Fig. 3 d) allows extracting the transmission line's loss α_Ω , shown in Fig. 3 f and the transmission line's refractive index, shown in Fig. 3 e. The extracted values agree well with the simulated values.

With experimental values for loss and refractive index now determined, a remaining parameter is the reflection

coefficient at the antenna-transmission line interface. Given the impedance mismatch between the antenna and the transmission line, a weak cavity is formed by the transmission line, with a reflectivity dictated by the antenna on one end and the open circuit termination on the other end, leading to fringes in the side-band ratio in Fig. 3 b. By comparing various $L_{TL}=0.25, 0.5$ and 1 mm we extract complex reflection coefficient of the antenna r_a , and by exploiting the fact that reflection losses are unaffected by L_{TL} , whereas propagation losses increase linearly with L_{TL} . We find a reflection coefficient ≈ 0.62 at 240-300 GHz and ≈ 0.73 around 100 GHz (see Fig. 3 g and h). Using these deduced parameters, we can model the experimental data shown in Fig. 2 e-f by applying eq. 1, which shows good agreement. Further details are provided in the methods and in the Supplementary Information section 5.

We note that the mmWave loss in our devices can be reduced by increasing the thickness of the transmission line electrodes (see Supplementary Information section 4). Additionally, the overall efficiency of the system can be further improved by enhancing the coupling between the THz wave and the transmission line through implementing broadband antennas (see Supplementary Information section 8).

High-speed mmWave detection

In the context of a 6G communication scheme, a mmWave signal serves as the carrier, with data packets encoded onto it via amplitude or phase modulation. This modulation process broadens the signal's bandwidth. Specifically, it extends the carrier's frequency range by twice the modulation frequency. Consequently, detecting the full span of this modulated mmWave signal requires a broadband device capable of covering the entire resulting frequency spectrum. This bandwidth requirement also applies to other applications such as high-speed mmWave sensing.

To verify our modulator's suitability for these applications, we now implement this device as a high-speed broadband mmWave detector. In this configuration, we amplitude modulate a 278.1 GHz carrier using a high-speed electronic mixer. To investigate the electronic bandwidth of our detector, we apply frequencies spanning from 10 MHz to 6 GHz to the mixer by connecting a RF source to the intermediate frequency (IF) port of the mixer. A sketch of the experimental setup is shown in Fig. 4 a.

In this configuration, the generated mmWave power is -21 dBm (vs +5 dBm in the previous experiments), limited by the power handling of the electronic mixer (-11 dBm of IF power to maintain <1 dB compression level) and its conversion loss (10 dB). Given the sideband ratio per mW of mmWave power (Fig. 2 e), we expect a sideband ratio of approximately -67 dB (vs -38 dB in the experiments we discuss above). To overcome these challenging power constraints, the optical signal is preamplified using an Erbium-Doped Fiber amplifier (EDFA), resulting in an increased input optical power of +20 dBm before the chip, thereby increasing the sideband power. We note that this frequency has been chosen arbitrarily and similar performance was observed for other carrier frequencies.

We investigate the bandwidth of our wireless phase modulators using configuration A (Fig. 2 b) while monitoring the optical spectrum after the modulator on a high-resolution optical spectrum analyzer. For an amplitude-modulated mmWave signal, we observe two peaks at frequencies $f_{mmW} - f_{mod}$ and $f_{mmW} + f_{mod}$ (Fig. 4 b). By sweeping the modulation frequency from 10 MHz to 6 GHz (currently limited by the RF mixer), we observe that the separation between the two peaks scales linearly with f_{mod} . The large modulation bandwidth of our modulators enables the amplitude of the sideband to remain relatively flat throughout the sweep making it suitable for applications such as 6G or high-speed mmWave/terahertz detection (Fig. 4 c).

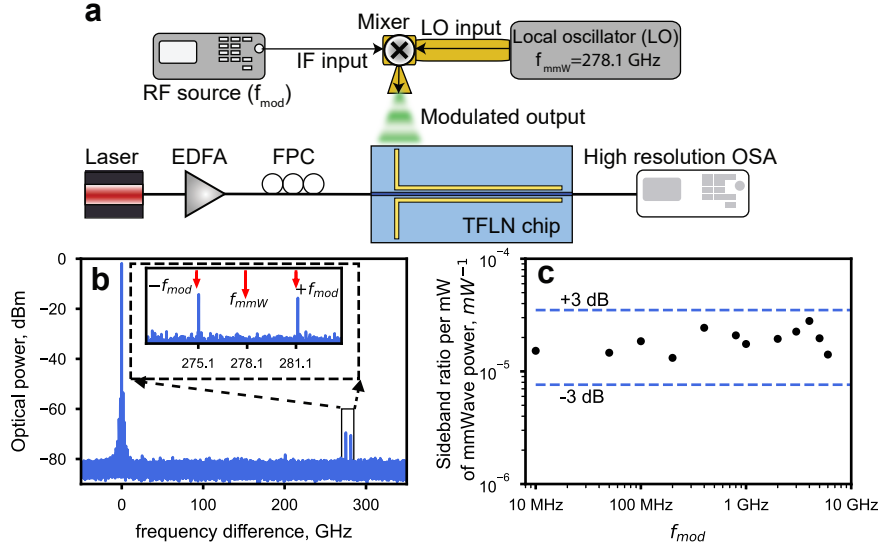


Fig. 4: Experimental results on high-speed detection of wireless mmWave radiation. (a) A sketch of the experimental setup used to characterize the response of our traveling wave electro-optic modulator under illumination with an intensity-modulated mmWave signal oscillating at 278.1 GHz. The modulation signal is sinusoidal, oscillates with a frequency f_{mod} and is generated by an RF source. An electronic mixer imprints the modulation signal onto the intensity of the mmWave signal. The mmWave is connected to the local oscillator (LO) port and the modulation signal is connected to the intermediate frequency (IF) port. An optical signal is coupled through the edge of the chip and the output spectrum is monitored on a high-resolution optical spectrum analyzer (OSA) after amplification with an erbium doped fiber amplifier (EDFA) and controlling its polarization using fiber components (FPC). (b) Optical spectrum at offset frequencies from the optical carrier, under illumination with a mmWave signal modulated at 3 GHz. Two optical tones are clearly visible, offset by f_{mmW} from the optical carrier and separated by $2 \cdot f_{mod}$, confirming efficient intensity modulation of the mmWave. As expected, this is accompanied by the suppression of the f_{mmW} tone. The incident free-space mmWave power was $7.65 \mu\text{W}$, the inset plot shows the zoomed region marked with a black rectangle; (c) Normalized sideband ratio as the function of modulation frequency, showing a flat modulation efficiency with frequency up to 6 GHz. Dashed lines represent ± 3 dB bounds.

MmWave electro-optic frequency combs

Apart from traveling-wave electro-optic modulators, cavity-based modulators play a pivotal role in advancing mmWave photonics. By enabling optical photons to make multiple round-trips within the cavity, these modulators significantly enhance photon-photon interaction probability compared to single-pass configurations. In particular, cavity-based modulation schemes enable applications such as electro-optic transduction [44] and ultra-sensitive field sensing [45] even under weak mmWave illumination. Under strong mmWave illumination, the generated photons can interact multiple times with the mmWave photons, leading to cascaded sideband generation and resulting in the formation of an optical frequency comb.

Resonant electro-optic frequency comb sources can be driven by the multiples of the optical cavity's FSR. In practice, this is not straightforward to do with conventional electronics due to technical challenges in realizing modulators operating up to hundreds of gigahertz bandwidth. However, our wideband modulator provides access to a broad range of frequencies. To achieve an electro-optic frequency comb we fabricate a racetrack resonator with a designed free-spectral range of the cavity be 30.79 GHz. We place a 1.5 mm-long mmWave antenna-coupled transmission line in one of the arms of the racetrack to phase modulate the light circulating in the cavity (Fig. 5 a). We use configuration A to characterise our mmWave electro-optic comb source. Give that

- the frequency of the optical radiation matches the resonant frequency of the cavity, and
- the frequency of the mmWave radiation matches $n \times \text{FSR}$, where n is an integer number and FSR is free

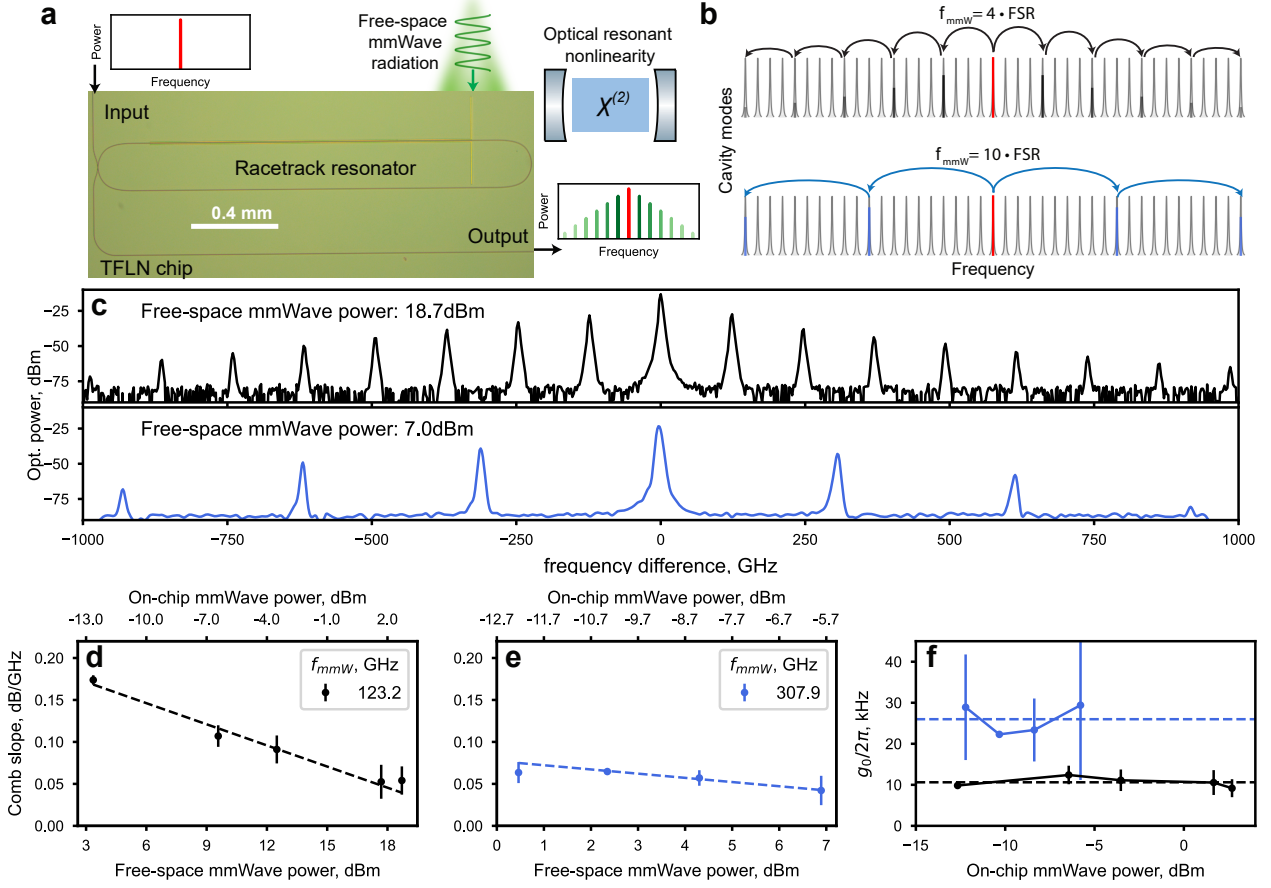


Fig. 5: Experimental results on wireless electro-optic comb generation. (a) A sketch of the setup. The continuous-wave laser pumps the racetrack resonator, and the laser's frequency matches to one of the racetrack's resonances. The chip is illuminated with the free-space mmWave radiation. The optical photon, passing multiple times the transmission line, has a higher chance to generate an up- or down-converted sideband. In turn, if the generated sideband becomes strong enough, it may interact with the mmWave photons again, leading to the cascading effect and generation of the electro-optic comb. This system might be represented as a $\chi^{(2)}$ in the optical resonator, leading to an optically enhanced resonant nonlinear interaction. (b) A representation of the cascaded electro-optic comb generation. The pumping laser (red line) pumps one of the optical resonances, and if the mmWave frequency f_{mmW} matches to an integer number times free-spectra range (FSR) of the racetrack, the generation process becomes cascading leading to a larger electro-optic bandwidth. (c) the measured output spectra out of the chip by shining mmWave radiation at frequencies of 123.2 GHz = 4 · FSR (upper plot, black line) and 307.9 GHz = 10 · FSR (bottom plot, blue line) at maximal mmWave free-space powers; the comb slopes as the function of mmWave power at (d) 123.2 GHz and (e) 307.9 GHz; the upper x-axis indicating the calculated mmWave on-chip power; (f) calculated single-photon coupling rate g_0 for 307.9 GHz (blue curve) and 123.2 GHz (black curve); the dashed lines show the mean value over the whole power range.

spectral range of the cavity,

the theoretical model shows that in the weak-pump regime, where electro-optic coupling strength (g_{eo}) is smaller than optical resonance linewidth (κ), the comb slope S [dB/GHz] is given by [46]:

$$S \approx -\frac{10}{f_{mmW}} \log_{10} \left(\frac{4g_{eo}^2}{\kappa^2} \right). \quad (2)$$

Here, $g_{eo} = g_0 \sqrt{n_{mmW}}$, with g_0 being single-photon electro-optic coupling rate and n_{mmW} is the number of mmWave photons in the transmission line.

We design the device to be under-coupled and measure its intrinsic linewidth to be $\kappa = 220$ MHz (see Supplementary Information Section 6). We record the output spectra of the racetrack resonator under two distinct illumination frequencies: 123.2 GHz, corresponding to 4×FSR, and 307.9 GHz, corresponding to 10×FSR of the ring (Fig. 5b). The comb offers a characteristic slope of 0.05 dB/GHz (Fig. 5 c) and span a bandwidth of approximately 2 THz.

We further verify that the comb slope scales with the incident free-space mmWave power at both illumination frequencies, showing a linear dependence consistent with Eq. 2 for both mmWave frequencies of 123.2 GHz as at 307.9 GHz (Fig. 5 d-e), see details in Supplementary Information section 7. However, we find that achieving the same slope requires a lower power at 307.9 GHz than at 123.2 GHz (e.g. 2 dBm at 123.2 GHz versus -5.7 dBm at 307.9 GHz), indicating that the efficiency of the comb generation per mW of mmWave power is larger at higher frequencies. We attribute this higher efficiency to the increased single-photon electro-optic coupling rate at higher frequencies, which scales as $g_0 \propto \sqrt{f_{mmW}}$ [46]. The estimated single-photon electro-optic coupling rates $g_0/2\pi$ from the experimental data are 10.61 ± 1.11 kHz and 25.99 ± 3.18 kHz at 123.2 and 307.9 GHz, respectively (Fig. 5 f). These values are approximately 10 times higher than the previous reports [15, 46] (see full analysis in Methods).

3 Conclusions and outlooks

In summary, we present a theoretical and experimental demonstration for a wireless electro-optic modulation scheme on the thin-film lithium niobate platform. In this approach, the mmWave radiation is coupled directly to the chip via an integrated antenna. This wireless coupling approach offers practical advantages eliminating the need for impedance-matched transmission lines and avoiding the complexity and cost associated with high-frequency mmWave probes. This wireless architecture offers a practical and scalable pathway for high-speed modulation in integrated photonic systems. We developed experimental design guidelines for implementing wireless modulators across broad mmWave frequency bands and introduced a photonics-based metrology technique to characterize key performance metrics, including the refractive index, transmission line loss, and the complex reflection coefficient at the antenna-transmission line interface. We demonstrated coupling efficiencies of up to 8% and showcased a path towards further improvement through antenna engineering. In addition, we demonstrated a reflection coefficient of ≈ 0.62 in the 240-300 GHz frequency range and ≈ 0.73 at frequencies around 100 GHz. This is particularly significant for the development of on-chip mmWave/terahertz cavities for quantum optics and quantum computing applications.

Furthermore, combining lithium niobate properties and strong mmWave confinement enabled a nearly tenfold enhancement in the single-photon electro-optic coupling rate g_0 , compared to previously reported values. A key challenge is reducing mmWave losses, for which we identify the use of thicker transmission lines as a promising solution. Notably, this issue can be partially alleviated in superconducting circuits, where resistive losses are inherently suppressed.

This novel architecture holds promise for broadening the scope and applicability of electro-optic modulators across a wide range of disciplines. By eliminating the need for direct electrical contact and enabling efficient free-space coupling, the wireless configuration not only simplifies system integration but also unlocks new opportunities in environments where conventional wired approaches are impractical or lossy. In particular, this approach is ideally suited for mmWave and terahertz sensing applications, where compact, high-bandwidth, and low-loss modulators are essential for detecting weak electromagnetic fields. Perhaps most compellingly, this platform opens new frontiers in quantum technologies. The ability to perform high-frequency electro-optic modulation without direct wiring could become relevant for emerging qubit platforms [17]. In such systems, minimizing thermal load, wiring density, and electromagnetic interference is critical, and the proposed wireless modulator offers a scalable path toward compact, low-noise quantum interfaces. As the demand for integrated photonic systems continues to grow across both classical and quantum domains, this wireless electro-optic architecture represents a foundational step toward enabling next-generation high-frequency photonic technologies.

Our results lay the foundation for compact, efficient, and scalable wireless electro-optic modulators, unlocking new possibilities in high-frequency sensing, free-space communication, and quantum information science.

4 Methods

Fabrication

The chips are fabricated on 600 nm of X-cut lithium niobate, bonded to 4700 nm of thermally grown oxide on an approximately 500 μm -thick double-side polished high-resistivity silicon substrate. The waveguides are patterned using electron-beam lithography (Eliionix ELS-HS50) and Ma-N resist. These waveguides are then etched into the LN layer using Ar^+ ions, followed by annealing in an O_2 environment to recover implantation damages and improve the absorption loss of the platform [47]. Subsequently, we clad the devices with 800 nm of Inductively Coupled Plasma - Chemical Vapor Deposition (Oxford Cobra), followed by another annealing. The electrodes are defined using a self-aligned process, including patterning with PMMA resist, dry etching, and lift-off using the same resist. The electrodes are deposited using electron-beam evaporation (Denton) with 15 nm of Ti and 300 nm of Au.

Experimental setup and measurements

The tunable Keysight N7776C laser generates a 1550 nm continuous wave 16 mW pump, which is then coupled by lensed fiber (OZ Optics TSMJ-X-1550-9/125-0.25-7-2.5-14-2) to the lithium niobate waveguide on the chip from the edge. The polarization is aligned to the TE mode of lithium niobate waveguide by a Thorlabs FPC561 Fiber Polarization Controller. In the measurements (section 2) of wireless electro-optic modulator bandwidth of the main text, there is also an EDFA (Erbium-Doped Fiber Amplifier) Nuphoton Technologies CW-C0-MR-30-20-FCA with a gain in power of 10. For the outcoupling we use (OZ Optics TSMJ-X-1550-9/125-0.25-7-2.5-28-5).

The mmWave radiation is generated the following way: an Anritsu RF/Microwave Signal Generator MG362x1A sends an RF signal (9-14 GHz) to the mmWave source (Virginia Diodes Signal Generator Extension module, WR9.0 + WR2.8), which provides a 9x or 27x frequency up-conversion and emits up to 100 mW in WR9.0 range and up to 5 mW in WR2.8 range. The mmWave radiation is emitted into the free space via a horn antenna (Virginia Diodes WR8.0CH antenna is used in the frequency range of 80-125 GHz with a beam waist at central frequency: 5.2 mm and WR2.8DH antenna in the frequency range of 240-380 GHz, beam waist at central frequency: 1.9 mm). In the configuration A of the text we use 1 inch aperture, 10 mm focal length TPX lens to tightly focus the mmWave beam on the silicon lens, while in the configuration B we used a pair of TPX lenses: the first one, with an aperture of 1 inch and focal length of 20mm, is used to form a collimated beam after the output of the horn antenna, and the second one, with a large 2 inch aperture and 65mm focal length is used to focus the beam on the silicon lens. Then mmWave radiation is collected by the on-chip antenna and coupled into the transmission line. Thus, the optical and THz modes co-propagate and mix, creating sidebands detected by the OSA (Anritsu Optical Spectrum Analyzer MS9740B). For the measurements in section 2 the high-resolution OSA (Apex AP2043B) was used. The Keysight MXG Vector Signal Generator was used to generate the modulation microwave signal for the experiment in section 2. A balanced mixer from Virginia Diodes (WR2.8BAMULP) was used to generate the modulated mmWave signal. The TPX lens from Batop (LTA-D25.4-F10) was used to focus free-space mmWave radiation on the chip. However, in section 2, for the measurements in configuration B, two lenses were used: first to collimate the mmWave beam (LTA-D25.4-F25), and then the second to focus the radiation on the chip (LTA-D50-F65). The Hyperhemispheric Silicon Lens from Batop

(LSH-D12-T7.13) was fixed on the back of the chip using a self-designed chip holder.

Photonics-enabled characterisation of mmWave transmission lines

We implement a photonics-enabled technique to extract the transmission line's parameters. Our method relies on analyzing the difference in sideband ratio $dSBR$ is given by the following formula:

$$dSBR = 10 \log_{10} \left(\frac{SBR_{forward}}{SBR_{backward}} \right) = 20 \cdot \log_{10} \left(\frac{\left| \frac{e^{i\Delta\tilde{k}_+ L_{TL}-1}}{\Delta\tilde{k}_+ L_{TL}} + e^{i2k_{\Omega} L_{TL} - \alpha_{\Omega} L_{TL}} \cdot \frac{e^{i\Delta\tilde{k}_- L_{TL}-1}}{\Delta\tilde{k}_- L_{TL}} \right|}{\left| \frac{e^{-i\Delta\tilde{k}_- L_{TL}-1}}{\Delta\tilde{k}_- L_{TL}} + e^{i2k_{\Omega} L_{TL} - \alpha_{\Omega} L_{TL}} \cdot \frac{e^{-i\Delta\tilde{k}_+ L_{TL}-1}}{\Delta\tilde{k}_+ L_{TL}} \right|} \right) \quad (3)$$

which depends on the phase matching in co-propagating and counter propagating configuration, respectively, expressed through $\Delta\tilde{k}_{\pm} = \frac{2\pi f_{mmW}}{c_0}(n_{\Omega} \mp n_g) \pm i\frac{\alpha_{\Omega}}{2}$. These two terms depend, in turn, on the terahertz refractive index $n_{\Omega} = n_0 + \frac{n'}{\sqrt{f_{mmW}}}$ where n_0 and n' are the fitting parameters, and the mmWave loss α_{Ω} . As we show in Supplementary Information 4, the main origin of the loss is the metallic loss caused by the finite surface impedance of the gold electrodes. Therefore α_{Ω} depends on f_{mmW} and σ_{Au} and geometrical parameters of the transmission line according to [48, 38, 39, 40]. We note that the second term of the expression for the mmWave refractive index originates from the complex part of the surface impedance, as was explored in [39]. n_g was kept to be 2.25 as measured in [36]. Fitting this formula to our experimental results helps retrieve the mmWave refractive index and propagation loss of the transmission line. Our fitted value of gold conductance $\sigma_{Au}^{fit} = 1.91 \cdot 10^7$ S/m, notably lower than the bulk value ($4.1 \cdot 10^7$ S/m), consistent with prior observations of evaporated thin films [49].

We extract the reflection coefficient at the antenna-transmission line interface as follows. As derived in the Supplementary Information 2, an impedance mismatch between the antenna and the transmission line will result in the mmWave signal being reflected at the antenna-transmission line interface, resulting in a weak cavity effect. The transmission line forms a resonator with a reflectivity dictated by the antenna on one end and the open circuit termination on the other end. The resonator acts as a filter and only mmWave fields oscillating at frequencies that match its cavity modes can efficiently couple to the resonator, leading in visible fringes in the side-band ratio. The visibility of these fringes correlates with the reflection coefficient at the antenna-transmission line interface. Consequently, comparing various L_{TL} allows extracting the complex reflection coefficient of the antenna r_a which affects the fringe visibility, since reflection losses are unaffected by L_{TL} , whereas propagation losses increase linearly with L_{TL} . According to our theoretical model, the reflection coefficient r_a might be extracted from:

$$\frac{SBR}{P_{mmW}^{free-space}} \propto \frac{PM^2 \cdot L_{TL}^2 \cdot \eta}{|1 - r_a e^{-\alpha_{\Omega} L_{TL}} e^{i \cdot 4\pi f_{mmW} n_{\Omega} L_{TL} / c_0}|^2} \quad (4)$$

We used three independent parameters of the fit: n_{Ω} , r_a , and a proportionality constant in the formula above. η was taken as the linear dependence shown in Supplementary Information 5.

Calculation of the single-photon coupling rate g_0 from the electro-optic comb slope

First, the electro-optic coupling rate g_{eo} was computed from the slope according to eq. 2. Then, the number of mmWave photons n_{mmW} in the traveling wave regime was estimated as follows [46]:

$$n_{mmW} = \frac{P_{mmW}^{on-chip}}{\hbar \cdot (2\pi f_{mmW})^2} \quad (5)$$

And then, g_0 is estimated as $g_{eo}/\sqrt{n_{mmW}}$ and plotted in Fig.5f. The errorbars for g_0 are calculated from the measurement error of the comb slope S .

Data Availability The data generated in this study will be made available in the Zenodo database prior to publication.

Code Availability The code used to plot the data within this paper will be made available in the Zenodo database prior to publication.

References

- [1] D. Tauber, B. Smith, D. Lewis, E. Muhigana, M. Nissov, D. Govan, J. Hu, Y. Zhou, J. Wang, W.-J. Jiang, et al. “Role of coherent systems in the next DCI generation.” *Journal of Lightwave Technology*, **41**(4):1139–1151 (2023).
- [2] Y. Huang, Y. Shen, and J. Wang. “From Terahertz Imaging to Terahertz Wireless Communications.” *Engineering*, **22**:106–124 (2023).
- [3] M. Haziq, S. Falina, A. A. Manaf, H. Kawarada, and M. Syamsul. “Challenges and opportunities for high-power and high-frequency AlGaIn/GaN high-electron-mobility transistor (HEMT) applications: A review.” *Micromachines*, **13**(12):2133 (2022).
- [4] W. KOU, S. LIANG, H. ZHOU, Y. DONG, S. GONG, Z. YANG, and H. ZENG. “A review of terahertz sources based on planar Schottky diodes.” *Chinese Journal of Electronics*, **31**(3):467–487 (2022).
- [5] T. Harter, C. Füllner, J. N. Kemal, S. Ummethala, J. L. Steinmann, M. Brosi, J. L. Hesler, E. Bründermann, A.-S. Müller, W. Freude, et al. “Generalized Kramers–Kronig receiver for coherent terahertz communications.” *Nature Photonics*, **14**(10):601–606 (2020).
- [6] S. Jia, L. Zhang, S. Wang, W. Li, M. Qiao, Z. Lu, N. M. Idrees, X. Pang, H. Hu, X. Zhang, et al. “ 2×300 Gbit/s line rate PS-64QAM-OFDM THz photonic-wireless transmission.” *Journal of Lightwave Technology*, **38**(17):4715–4721 (2020).
- [7] F. Meng and N. Zhu. “An MSCL-based attenuator with ultralow insertion loss and intrinsic ESD-protection for millimeter-wave and terahertz applications.” *IEEE Transactions on Microwave Theory and Techniques*, **71**(1):240–249 (2022).
- [8] C. Wang, D. Fang, J. Zhang, A. Kotz, G. Lihachev, M. Churaev, Z. Li, A. Schwarzenberger, X. Ou, C. Koos, et al. “Ultrabroadband thin-film lithium tantalate modulator for high-speed communications.” *Optica*, **11**(12):1614–1620 (2024).
- [9] Y. Horst, D. Moor, D. Chelladurai, T. Blatter, S. Fernandes, L. Kulmer, M. Baumann, H. Ibili, C. Funck, K. Keller, et al. “Ultra-wideband MHz to THz plasmonic EO modulator.” *Optica*, **12**(3):325–328 (2025).
- [10] M. Zhang, C. Wang, P. Kharel, D. Zhu, and M. Lončar. “Integrated lithium niobate electro-optic modulators: when performance meets scalability.” *Optica*, **8**(5):652–667 (2021).
- [11] S. Zhu, Y. Zhang, J. Feng, Y. Wang, K. Zhai, H. Feng, E. Y. B. Pun, N. H. Zhu, and C. Wang. “Integrated lithium niobate photonic millimetre-wave radar.” *Nature Photonics*, pages 1–8 (2025).

- [12] Y. Yamaguchi, P. T. Dat, S. Takano, M. Motoya, S. Hirata, Y. Kataoka, J. Ichikawa, R. Shimizu, N. Yamamoto, K. Akahane, et al. “Advanced optical modulators for sub-THz-to-optical signal conversion.” *IEEE Journal of Selected Topics in Quantum Electronics*, **29**(5: Terahertz Photonics):1–8 (2023).
- [13] N. Couture, F. Bouchard, A. Sit, G. Thekkadath, D. England, P. J. Bustard, and B. J. Sussman. “Terahertz electro-optic modulation of single photons.” *arXiv preprint arXiv:2503.19667* (2025).
- [14] G. Santamaría Botello, F. Sedlmeir, A. Rueda, K. A. Abdalmalak, E. R. Brown, G. Leuchs, S. Preu, D. Segovia-Vargas, D. V. Strekalov, L. E. García Muñoz, et al. “Sensitivity limits of millimeter-wave photonic radiometers based on efficient electro-optic upconverters.” *Optica*, **5**(10):1210–1219 (2018).
- [15] K. K. Multani, J. F. Herrmann, E. A. Nanni, and A. H. Safavi-Naeini. “Integrated sub-terahertz cavity electro-optic transduction.” *arXiv preprint arXiv:2504.01920* (2025).
- [16] L. Yi, Y. Li, and T. Nagatsuma. “Photonic radar for 3D imaging: From millimeter to terahertz waves.” *IEEE Journal of Selected Topics in Quantum Electronics*, **29**(5: Terahertz Photonics):1–14 (2023).
- [17] A. Anferov, F. Wan, S. P. Harvey, J. Simon, and D. I. Schuster. “A Millimeter-Wave Superconducting Qubit.” *arXiv preprint arXiv:2411.11170* (2024).
- [18] A. Kumar, A. Suleymanzade, M. Stone, L. Taneja, A. Anferov, D. I. Schuster, and J. Simon. “Quantum-enabled millimetre wave to optical transduction using neutral atoms.” **615**(7953):614–619.
- [19] A. Suleymanzade, A. Anferov, M. Stone, R. K. Naik, A. Oriani, J. Simon, and D. Schuster. “A tunable high-Q millimeter wave cavity for hybrid circuit and cavity QED experiments.” *Applied Physics Letters*, **116**(10):104001 (2020).
- [20] S. Rajabali and I.-C. Benea-Chelms. “Present and future of terahertz integrated photonic devices.” *APL Photonics*, **8**(8):080901 (2023).
- [21] C. Wang, M. Zhang, B. Stern, M. Lipson, and M. Lončar. “Nanophotonic lithium niobate electro-optic modulators.” *Optics express*, **26**(2):1547–1555 (2018).
- [22] A. J. Mercante, S. Shi, P. Yao, L. Xie, R. M. Weikle, and D. W. Prather. “Thin film lithium niobate electro-optic modulator with terahertz operating bandwidth.” *Optics express*, **26**(11):14810–14816 (2018).
- [23] M. Xu, M. He, H. Zhang, J. Jian, Y. Pan, X. Liu, L. Chen, X. Meng, H. Chen, Z. Li, et al. “High-performance coherent optical modulators based on thin-film lithium niobate platform.” *Nature communications*, **11**(1):3911 (2020).
- [24] S. H. Badri, M. V. Kotlyar, R. Das, Y. Arafat, O. Moynihan, B. Corbett, L. O’Faolain, and S. Ghosh. “Compact modulators on silicon nitride waveguide platform via micro-transfer printing of thin-film lithium niobate.” **15**(1):11681.
- [25] P. Zhang, H. Huang, Y. Jiang, X. Han, H. Xiao, A. Frigg, T. G. Nguyen, A. Boes, G. Ren, Y. Su, et al. “High-speed electro-optic modulator based on silicon nitride loaded lithium niobate on an insulator platform.” *Optics letters*, **46**(23):5986–5989 (2021).

- [26] Y. Salamin, W. Heni, C. Haffner, Y. Fedoryshyn, C. Hoessbacher, R. Bonjour, M. Zahner, D. Hillerkuss, P. Leuchtmann, D. L. Elder, et al. “Direct conversion of free space millimeter waves to optical domain by plasmonic modulator antenna.” *Nano letters*, **15**(12):8342–8346 (2015).
- [27] Y. Salamin, I.-C. Benea-Chelms, Y. Fedoryshyn, W. Heni, D. L. Elder, L. R. Dalton, J. Faist, and J. Leuthold. “Compact and ultra-efficient broadband plasmonic terahertz field detector.” *Nature communications*, **10**(1):5550 (2019).
- [28] J. D. Witmer, T. P. McKenna, P. Arrangoiz-Arriola, R. Van Laer, E. A. Wollack, F. Lin, A. K. Jen, J. Luo, and A. H. Safavi-Naeini. “A silicon-organic hybrid platform for quantum microwave-to-optical transduction.” *Quantum Science and Technology*, **5**(3):034004 (2020).
- [29] P. Gräupner, J. Pommier, A. Cachard, and J. Coutaz. “Electro-optical effect in aluminum nitride waveguides.” *Journal of applied physics*, **71**(9):4136–4139 (1992).
- [30] D. Chelladurai, M. Kohli, J. Winiger, D. Moor, A. Messner, Y. Fedoryshyn, M. Eleraky, Y. Liu, H. Wang, and J. Leuthold. “Barium titanate and lithium niobate permittivity and Pockels coefficients from megahertz to sub-terahertz frequencies.” *Nature Materials*, pages 1–8 (2025).
- [31] A. Majkić, U. Puc, A. Franke, R. Kirste, R. Collazo, Z. Sitar, and M. Zgonik. “Optical properties of aluminum nitride single crystals in the THz region.” *Optical Materials Express*, **5**(10):2106–2111 (2015).
- [32] F. Wan, J. Han, and Z. Zhu. “Dielectric response in ferroelectric BaTiO₃.” *Physics Letters A*, **372**(12):2137–2140 (2008).
- [33] M. Wang, Y. Chen, S. Zhang, L. Dong, H. Yao, H. Xu, K. Chen, and J. Wu. “Perspectives of thin-film lithium niobate and electro-optic polymers for high-performance electro-optic modulation.” *Journal of Materials Chemistry C*, **11**(33):11107–11122 (2023).
- [34] I.-C. Benea-Chelms, M. L. Meretska, D. L. Elder, M. Tamagnone, L. R. Dalton, and F. Capasso. “Electro-optic spatial light modulator from an engineered organic layer.” *Nature communications*, **12**(1):5928 (2021).
- [35] A. Herter, A. Shams-Ansari, F. F. Settembrini, H. K. Warner, J. Faist, M. Lončar, and I.-C. Benea-Chelms. “Terahertz waveform synthesis in integrated thin-film lithium niobate platform.” *Nature Communications*, **14**(1):11 (2023).
- [36] Y. Lampert, A. Shams-Ansari, A. Gaier, A. Tomasino, S. Rajabali, L. Magalhaes, M. Lončar, and I.-C. Benea-Chelms. “Photonics-integrated terahertz transmission lines.” *arXiv preprint arXiv:2406.15651* (2024).
- [37] A. Tomasino, A. Shams-Ansari, M. Lončar, and I.-C. Benea-Chelms. “Large-area photonic circuits for terahertz detection and beam profiling.” *arXiv preprint arXiv:2410.20407* (2024).
- [38] W. Gallagher, C.-C. Chi, I. Duling III, D. Grischkowsky, N. Halas, M. Ketchen, and A. Kleinsasser. “Sub-picosecond optoelectronic study of resistive and superconductive transmission lines.” *Applied physics letters*, **50**(6):350–352 (1987).
- [39] U. D. Keil, D. R. Dykaar, A. Levi, R. F. Kopf, L. Pfeiffer, S. B. Darack, and K. West. “High-speed coplanar transmission lines.” *IEEE journal of quantum electronics*, **28**(10):2333–2342 (1992).

- [40] F. Martin. Artificial transmission lines for RF and microwave applications. John Wiley & Sons (2015).
- [41] H. Murata, H. Yokohashi, S. Matsukawa, M. Sato, M. Onizawa, and S. Kurokawa. “Antenna-coupled electrode electro-optic modulator for 5G mobile applications.” *IEEE Journal of Microwaves*, **1**(4):902–907 (2021).
- [42] H. Murata. “Millimeter-wave-band electro-optic modulators using antenna-coupled electrodes for microwave photonic applications.” *Journal of Lightwave Technology*, **38**(19):5485–5491 (2020).
- [43] C. Wang, M. Zhang, X. Chen, M. Bertrand, A. Shams-Ansari, S. Chandrasekhar, P. Winzer, and M. Lončar. “Integrated lithium niobate electro-optic modulators operating at CMOS-compatible voltages.” *Nature*, **562**(7725):101–104 (2018).
- [44] L. Fan, C.-L. Zou, R. Cheng, X. Guo, X. Han, Z. Gong, S. Wang, and H. X. Tang. “Superconducting cavity electro-optics: A platform for coherent photon conversion between superconducting and photonic circuits.” *Science Advances*, **4**(8):eaar4994 (2018).
- [45] X. Ma, Z. Cai, C. Zhuang, X. Liu, Z. Zhang, K. Liu, B. Cao, J. He, C. Yang, C. Bao, and R. Zeng. “Integrated microcavity electric field sensors using Pound-Drever-Hall detection.” *Nature Communications*, **15**(1):1386 (2024).
- [46] J. Zhang, C. Wang, C. Denney, J. Riemensberger, G. Lihachev, J. Hu, W. Kao, T. Blésin, N. Kuznetsov, Z. Li, et al. “Ultrabroadband integrated electro-optic frequency comb in lithium tantalate.” *Nature*, pages 1–8 (2025).
- [47] A. Shams-Ansari, G. Huang, L. He, Z. Li, J. Holzgrafe, M. Jankowski, M. Churaev, P. Kharel, R. Cheng, D. Zhu, N. Sinclair, B. Desiatov, M. Zhang, T. J. Kippenberg, and M. Lončar. “Reduced material loss in thin-film lithium niobate waveguides.” *APL Photonics*, **7**(8):081301 (2022).
- [48] G. Hasnain, A. Dienes, and J. Whinnery. “Dispersion of picosecond pulses in coplanar transmission lines.” *IEEE Transactions on Microwave Theory and Techniques*, **34**(6):738–741 (1986).
- [49] Y. Lee, D. Kim, J. Jeong, J. Kim, V. Shmid, O. Korotchenkov, P. Vasa, Y.-M. Bahk, and D.-S. Kim. “Enhanced terahertz conductivity in ultra-thin gold film deposited onto (3-mercaptopropyl) trimethoxysilane (MPTMS)-coated Si substrates.” **9**(1):15025.

Acknowledgments A.G., Y.L., and I.C.B.C. acknowledge funding from the European Union’s Horizon Europe research and innovation programme under project MIRAQLS with grant agreement No. 101070700 and funding from the Swiss National Science Foundation Grant No. №219406. S.R. acknowledges funding from the Hans Eggenberger Foundation (independent research grant 2022, Switzerland) and the Swiss National Science Foundation (Postdoc Mobility, grant number 214483). L.M. acknowledges funding from the Behring Foundation and CAPES-Fulbright.

Author contributions A.G. and I.C.B.C. conceptualized the project. A.G. and K.M. built the optical setup, carried out the measurements, and performed the CST simulations. A.G. derived the theoretical description of the modulation efficiency. Y.L. designed the layout of the photonic chip. J.L. helped with the measurements of the electro-optic combs. A.S.-A., S.R., and L.M. fabricated the devices. A.G., A.S.-A. and I.C.B.C wrote the manuscript with feedback from all authors. I.C.B.C. and M.L. supervised this work.

Competing interests The authors declare no competing interests.

Disclaimer The views, opinions and/or findings expressed are those of the author and should not be interpreted as representing the official views or policies of the Department of Defense or the U.S. Government.

Corresponding authors Correspondence to Aleksei Gaier (aleksei.gaier@epfl.ch) or Ileana-Cristina Benea-Chelmus (cristina.benea@epfl.ch).

Supplementary information for

Large-area photonic circuits for terahertz detection and beam profiling

A. Gaier, K. Mamian, S. Rajabali, Y. Lampert, J. Liu, L. Magalhaes, A. Shams-Ansari, M. Lončar, I.-C. Benea-Chelmus

Contents

1	Chip structure details	2
2	Theoretical model	3
2.1	Amplitude of the mmWave electric field coupled into transmission line from free-space	5
2.2	Relation between voltage and electric field amplitudes	6
3	Loss model	8
4	Co- and counter-propagation mmWave radiation inside the transmission line	8
5	Measurements of the antenna-transmission line reflection coefficient	9
6	Linewidth of the optical microring resonance	10
7	Measurements of the coupling efficiency for the experiment with the ring resonators	11
8	Strategies on improving the coupling efficiency of the mmWave radiation to the chip	11

1 Chip structure details

Details on the geometry of the measured and simulated devices are given in SI Fig. 1, and all dimensions are provided in SI Table 1. The refractive index of lithium niobate, silicon, and silicon oxide is calculated using the Lorentz model from [refs].

thickness of the high resistivity silicon substrate	h_{Si}	500 μm
thickness of the silicon oxide layer	h_{SiO_2}	4.7 μm
thickness of thin-film lithium niobate layer	h_{TF}	300 nm
thickness of the gold layer	h_{Au}	300 nm
height of the lithium niobate waveguide	h_{wg}	600 nm
thickness of the silicon oxide cladding	h_{clad}	1 μm
width of the lithium niobate waveguide	w_{wg}	1.5 μm
etching angle of the lithium niobate waveguide	θ_{wg}	60°
distance between the electrodes	w	3.3 μm
width of the antenna	w_a	5 μm
width of the gold layer inside the transmission line	w_{TL}	3.5 μm
length of the transmission line	L_{TL}	0.25-2 mm
length of the dipole antenna	L_a	400 μm

Tab. 1: Dimensions of the simulated and fabricated devices

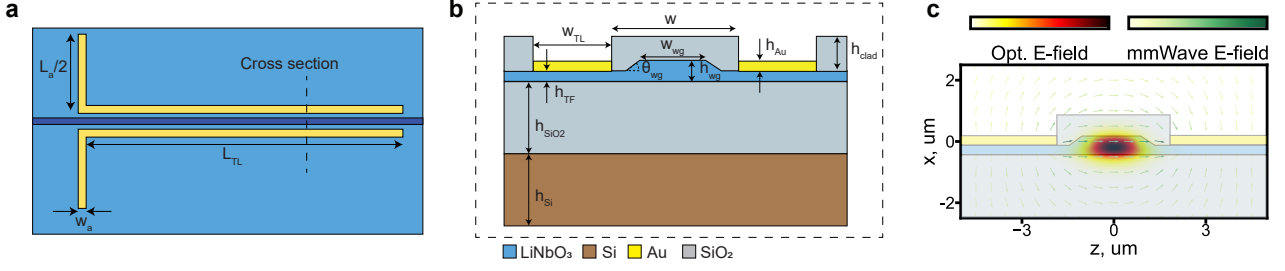


Fig. 1: (a) Top view of the dipole antenna devices showing the transmission line with length L_{TL} . (b) Cross-section of the fabricated chips. (c) Simulated 2-D profiles of the optical and mmWave modes.

2 Theoretical model

In this chapter, we developed a theoretical description of the interaction of mmWave radiation coupled to the transmission line. Namely, due to the nonlinear mixing of optical mode (at frequency ω_p) with mmWave field (at frequency Ω), the sidebands at frequencies $\omega_p \pm \Omega$ are generated.

We consider the linearly polarized optical fields along the z -axis, propagating along the y -axis. Then, the electric field might be written as follows:

$$E_{opt}(x, y, z, t) = \frac{1}{2} A(y) g_{opt}(x, z) e^{i(ky - \omega t)} + c.c. \quad (1)$$

where $A(y)$ is the amplitude of the electric field, $k = n_o \frac{\omega}{c_0}$ is the propagation constant of the optical eigenmode with the effective refractive index n_o and speed of light in vacuum c_0 , $g_{opt}(x, z)$ is a 2D field profile of the eigenmode of the waveguide, normalized in the following way: $\iint |g_{opt}|^2(x, z) dx dz = S_{opt}$, where S_{opt} is the effective mode area. We can assume that the nonlinear interaction is weak, which implies the non-depletion case of the optical probe, which means that the probe field E_p and the sideband E_{SB} could be described as follows:

$$E_p(x, y, z, t) = \frac{1}{2} A_p g_{opt}(x, z) e^{i(k_p y - \omega_p t)} + c.c. \quad (2)$$

here we neglect the probe depletion due to the nonlinear interaction; note that $A_p = \text{const}$ with respect to y , where the subscript "p" stands for the probe mode.

$$E_{SB}^{(\pm)}(x, y, z, t) = \frac{1}{2} A_{SB(\pm)}(y) g_{opt}(x, z) e^{i(k_{SB(\pm)} y - \omega_{SB(\pm)} t)} + c.c. \quad (3)$$

where $\omega_{SB(\pm)} = \omega_p \pm \Omega$, subscript "SB" stands for sideband mode, superscript (\pm) stands for the upconverted (+) and downconverted (-) sideband modes. The mmWave electric field (also linearly polarized along z -axis) can be described as follows:

$$E_{\Omega}(x, y, z, t) = \frac{1}{2} A_{\Omega} g_{\Omega}(x, z) e^{i(k_{\Omega} y - \Omega t)} e^{-\frac{\alpha_{\Omega}}{2} y} + \frac{1}{2} A_{\Omega}^{-} g_{\Omega}(x, z) e^{-i(k_{\Omega} y + \Omega t)} e^{\frac{\alpha_{\Omega}}{2} y} + c.c. \quad (4)$$

where $k_{\Omega} = n_{\Omega} \frac{\Omega}{c_0}$ is the wave vector of the RF wave with an effective refractive index n_{Ω} , α_{Ω} is the propagation loss of the mmWave radiation, and A_{Ω} and A_{Ω}^{-} are the amplitudes of the mmWave waves that co- and counter-propagate with an optical waves. Here we neglect the depletion of the mmWave amplitude due to the nonlinear interaction. The 2D profile of the mmWave mode is given by g_{Ω} function, which is normalized in the same way as g_{opt} : $\iint |g_{\Omega}|^2(x, z) dx dz = S_{\Omega}$.

The evolution of the optical electric field $E = E_p + E_{SB+} + E_{SB-}$ is given by the nonlinear wave equation:

$$\left(\nabla^2 - \frac{1}{c_0^2} \frac{\partial^2}{\partial t^2} \right) E(x, y, z, t) = \frac{1}{\epsilon_0 c_0^2} \frac{\partial^2}{\partial t^2} (\mathcal{P}^L(x, y, z, t) + \mathcal{P}^{NL}(x, y, z, t)) \quad (5)$$

where $\mathcal{P}^L(x, y, z, t) = \varepsilon_0 \int_{-\infty}^t \chi^{(1)}(x, y, z, t - t') E(x, y, z, t') dt'$ is the linear part of the polarization with $\chi^{(1)}$ being linear susceptibility, and $\mathcal{P}^{NL}(x, y, z, t) = \varepsilon_0 \chi^{(2)}(x, y, z, t) \cdot (E(x, y, z, t) + E_\Omega(x, y, z, t))^2$ is the nonlinear part of the polarization with $\chi^{(2)}$ being second-order nonlinear susceptibility. To simplify the expression for linear polarization, assuming the homogeneity of the material properties along the y-axis and using the properties of the Fourier transform, one may obtain:

$$\begin{aligned} \mathcal{P}^L(x, y, z, t) &= \varepsilon_0 \int_{-\infty}^t \chi^{(1)}(x, z, t - t') E(x, y, z, t') dt' = \\ &\frac{1}{2} \varepsilon_0 \chi^{(1)}(x, z, \omega_p) A_p g_{opt}(x, z) \cdot e^{i(k_p y - \omega_p t)} + \\ &\frac{1}{2} \varepsilon_0 \chi^{(1)}(x, z, \omega_{SB+}) A_{SB+}(y) g_{opt}(x, z) \cdot e^{i(k_{SB+} y - \omega_{SB+} t)} + \\ &\frac{1}{2} \varepsilon_0 \chi^{(1)}(x, z, \omega_{SB-}) A_{SB-}(y) g_{opt}(x, z) \cdot e^{i(k_{SB-} y - \omega_{SB-} t)} + c.c. \end{aligned} \quad (6)$$

Computing the second derivatives and using orthogonality of the complex exponents $\int e^{i(\omega - \omega')t} dt = 2\pi \delta(\omega - \omega')$, we can rewrite the equation 5 to describe the evolution of the (+) sideband:

$$\begin{aligned} &\left(\nabla^2 + \frac{\omega_{SB+}^2}{c_0^2} n^2(x, z, \omega_{SB+}) \right) A_{SB+}(y) \cdot g_{opt}(x, z) \cdot e^{ik_{SB+} y} = \\ &-\frac{2\chi^{(2)}(x, z) \omega_{SB+}^2}{c_0^2} A_p g_{opt}(x, z) g_\Omega(x, z) \left(A_\Omega e^{-\frac{\alpha_\Omega}{2} y} e^{i(k_p + k_\Omega)y} + A_\Omega^- e^{\frac{\alpha_\Omega}{2} y} e^{i(k_p - k_\Omega)y} \right) \end{aligned} \quad (7)$$

Now, we can split the nabla operator into longitudinal and transversal components: $\nabla^2 = \Delta_\perp^2 + \frac{\partial^2}{\partial y^2}$, so that:

$$\left(\nabla^2 + \frac{\omega_{SB+}^2}{c_0^2} n^2(x, z, \omega_{SB+}) \right) g_{opt}(x, z) = \left(\frac{\partial^2}{\partial y^2} + \left(\frac{\omega_{SB+}}{c_0} n_o \right)^2 \right) g_{opt}(x, z) \quad (8)$$

Now, by multiplying both sides of the equation by $g_{opt}(x, z)$ and integrating over the (x, z) coordinates, one may obtain:

$$\left(\frac{\partial^2}{\partial y^2} + \frac{\omega_{SB+}^2}{c_0^2} n_o^2 \right) A_{SB+}(y) \cdot e^{ik_{SB+} y} = -\frac{2\chi^{(2)} \omega_{SB+}^2}{c_0^2} A_p \Gamma_{eo} \left(A_\Omega e^{-\frac{\alpha_\Omega}{2} y} e^{i(k_p + k_\Omega)y} + A_\Omega^- e^{\frac{\alpha_\Omega}{2} y} e^{i(k_p - k_\Omega)y} \right) \quad (9)$$

where we introduced the spatial overlap factor as follows:

$$\Gamma_{eo} = \frac{\iint_{LN} g_{opt}^2(x, z) \cdot g_\Omega(x, z) dx dz}{\iint_{x,z} g_{opt}^2(x, z) dx dz} \quad (10)$$

where the integral in the nominator is taken over the nonlinear medium (in our case, lithium niobate waveguide), and the area of the integral in the denominator is the whole XZ plane, and we introduced effective nonlinear susceptibility $\chi^{(2)} = \chi_{333}^{(2)}$. Calculating the second derivatives in the left part of the equation gives:

$$\left(\frac{\partial^2}{\partial y^2} + \frac{\omega_{SB+}^2}{c_0^2} n_o^2 \right) A_{SB+}(y) \cdot e^{ik_{SB+} y} = e^{ik_{SB+} y} \cdot \left(\frac{\partial^2 A_{SB+}}{\partial y^2} + 2ik_{SB+} \frac{\partial A_{SB+}}{\partial y} \right) \quad (11)$$

Substituting this result into the nonlinear wave equation gives:

$$\frac{\partial^2 A_{SB+}}{\partial y^2} + 2ik_{SB+} \frac{\partial A_{SB+}}{\partial y} = -\frac{2\chi^{(2)} \omega_{SB+}^2}{c_0^2} A_p \Gamma_{eo} \left(A_\Omega e^{-\frac{\alpha_\Omega}{2} y} e^{i\Delta\tilde{k}_+ y} + A_\Omega^- e^{\frac{\alpha_\Omega}{2} y} e^{i\Delta\tilde{k}_- y} \right) \quad (12)$$

where we introduced $\Delta\tilde{k}_\pm = \frac{2\pi f_{mmw}}{c_0} (n_\Omega \mp n_g) \pm i\frac{\alpha_\Omega}{2}$, with the group index of the optical mode n_g . If now we apply the slowly varying envelope approximation assuming $|\frac{\partial^2 A_{SB+}}{\partial y^2}| \ll |2k_{SB+} \frac{\partial A_{SB+}}{\partial y}|$ for eq. 12:

$$\frac{\partial A_{SB+}}{\partial y} = i\frac{\chi^{(2)} \omega_{SB+}}{c_0 n_o} A_p \Gamma_{eo} \cdot \left(A_\Omega e^{-\frac{\alpha_\Omega}{2} y} e^{i\Delta\tilde{k}_+ y} + A_\Omega^- e^{\frac{\alpha_\Omega}{2} y} e^{i\Delta\tilde{k}_- y} \right) \quad (13)$$

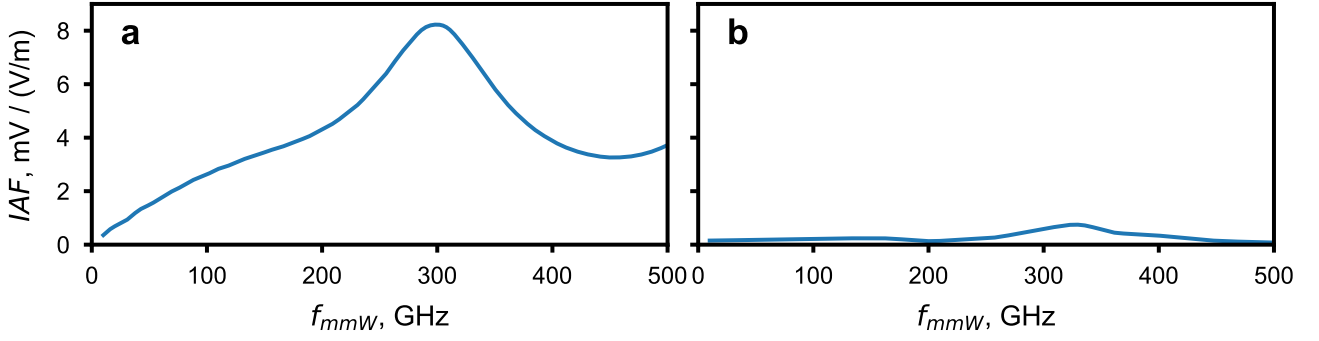


Fig. 2: Simulated inverse antenna factors for the antenna design used in this work in two configurations: with (a) and without (b) Si lens.

The solution of this equation at coordinate $y=L$, assuming that at $y=0$ the sideband mode is not populated, or in other words that $A_{SB+}(y=0) = 0$, is given by:

$$A_{SB+} = \frac{\chi^{(2)}\omega_{SB+}}{n_o c_0} A_p \Gamma_{eo} L \cdot \left(A_\Omega \frac{e^{i\Delta\tilde{k}_+ L} - 1}{\Delta\tilde{k}_+ L} + A_\Omega^- \frac{e^{i\Delta\tilde{k}_- L} - 1}{\Delta\tilde{k}_- L} \right) \quad (14)$$

This solution is valid only for small modulation, i.e., $|A_{SB+}| \ll |A_p|$. However, in practice, the coherence length $L_{coh}^- = \frac{\pi}{\Delta\tilde{k}_-} \ll L$ at frequencies above 100 GHz, and therefore the contribution of the second term is negligible:

$$A_{SB+} = \frac{\chi^{(2)}\omega_{SB+}}{n_o c_0} A_p \Gamma_{eo} L \cdot A_\Omega \frac{e^{i\Delta\tilde{k} L} - 1}{\Delta\tilde{k} L} \quad (15)$$

where we set $\Delta\tilde{k}_+ = \Delta\tilde{k}$. The next step is to find the relation between the incident free-space mmWave electric field E_{inc} and the amplitude A_Ω of mmWave electric field mode coupled to the transmission line. In the next section, we will evaluate the amplitude of the mmWave electric field in the transmission line upon illumination with free-space mmWave radiation.

2.1 Amplitude of the mmWave electric field coupled into transmission line from free-space

The incident electric field E_{inc} induces a voltage between antenna pads, which depends on the inverse antenna factor (IAF):

$$V_a = IAF \cdot E_{inc} \quad (16)$$

The values of the inverse antenna factor for the antenna used in this work is shown in Fig.2. It has a clear resonance at center frequency ≈ 300 GHz, and reaching the value of 8 mV/(V/m). In this plot we compared two ways of the antenna illumination: with and without silicon lens. Adding the silicon lens improved the antenna factor almost ten folds. However, in practice, only if the input beam waist is much larger than the antenna aperture this formula apply. In the case, for example, of antenna illumination with a gaussian beam with a waist smaller than the silicon lens aperture, this value may differ from the simulated values and should be studied for the parameters of the input beam.

The voltage generated by the antenna launches a voltage wave into the transmission line, and the relation between antenna voltage and the transmission line is studied below.

2.2 Relation between voltage and electric field amplitudes

Consider the equivalent circuit for the devices with the antenna placed at the beginning of the transmission line shown in Fig. 3, where the line is terminated with a reflection coefficient r at $y = L$. Antenna serves as a voltage generator with V_a and Z_a . The present circuit could be studied using an infinite series to represent the multiple bounces from both ends of the transmission line, however for the sake of simplicity we will use the method of impedance transformation described in [1]. The voltage and current in the line are given by the superposition of the waves flowing in the positive and negative directions along the transmission line:

$$V(y) = V_0^+ e^{-\gamma y} + V_0^- e^{\gamma y}, \quad (17)$$

$$I(y) = \frac{1}{Z_{TL}} (V_0^+ e^{-\gamma y} - V_0^- e^{\gamma y}), \quad (18)$$

The reflection coefficient r at the load ($y = L$) is the ratio of amplitudes of the left-traveling wave and the right-

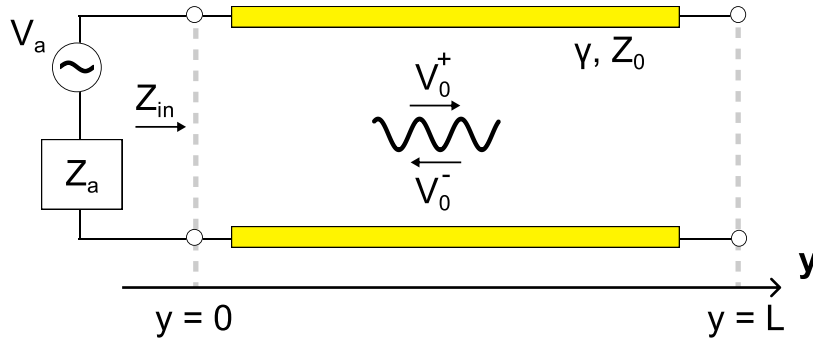


Fig. 3: Equivalent circuit scheme for the devices under study. The antenna serves as a voltage generator connected in series to the transmission line. The reflection coefficient r from the end of the transmission line is close to 1, thus an open circuit termination is schematically shown.

traveling one:

$$r = \frac{V_0^- e^{\gamma L}}{V_0^+ e^{-\gamma L}} = \frac{V_0^-}{V_0^+} e^{2\gamma L} \quad (19)$$

Putting this expression into the ones above gives:

$$V(y) = V_0^+ (e^{-\gamma y} + r e^{-2\gamma L} e^{\gamma y}), \quad (20)$$

$$I(y) = \frac{V_0^+}{Z_{TL}} (e^{-\gamma y} - r e^{-2\gamma L} e^{\gamma y}), \quad (21)$$

$$Z_{in}(y=0) = \frac{V(0)}{I(0)} = Z_{TL} \frac{1 + r e^{-2\gamma L}}{1 - r e^{-2\gamma L}}, \quad (22)$$

where $\gamma = \frac{\alpha_\Omega}{2} - i k_\Omega$ ($\alpha_\Omega > 0$) is the complex propagation constant of the mmWave mode, Z_{TL} is the characteristic impedance of the line.

Since the phase-matching condition is satisfied primarily for the right-traveling wave, further we are interested in V_0^+ . To find V_0^+ we note that on the one hand, $V(0) = V_0^+ (1 + r e^{-2\gamma L})$; on the other hand, from the antenna side we can write based on the expression for impedances connected in series: $V(0) = V_a \frac{Z_{in}}{Z_{in} + Z_a}$. Equating these two expressions for $V(0)$ we get:

$$V_0^+ = V_a \frac{Z_{in}}{Z_{in} + Z_a} \frac{1}{1 + r e^{-2\gamma L}} \quad (23)$$

It's useful to rewrite eq. 23 in terms of reflection coefficients from both ends:

$$\begin{aligned}
V_0^+ &= V_a \frac{Z_{in}}{Z_{in} + Z_a} \frac{1}{1 + re^{-2\gamma L}} = V_a \frac{Z_{TL} \frac{1+re^{-2\gamma L}}{1-re^{-2\gamma L}}}{Z_{TL} \frac{1+re^{-2\gamma L}}{1-re^{-2\gamma L}} + Z_a} \frac{1}{1 + re^{-2\gamma L}} = V_a \frac{Z_{TL} \frac{1}{1-re^{-2\gamma L}}}{Z_{TL} \frac{1+re^{-2\gamma L}}{1-re^{-2\gamma L}} + Z_a} = \\
&= V_a \frac{Z_{TL}}{Z_{TL}(1 + re^{-2\gamma L}) + Z_a(1 - re^{-2\gamma L})} = V_a \frac{Z_{TL}}{Z_{TL} + Z_a + re^{-2\gamma L}(Z_{TL} - Z_a)} = \\
&= V_a \frac{Z_{TL}}{Z_{TL} + Z_a} \frac{1}{1 - r \cdot r_a e^{-2\gamma L}} = \frac{V_a}{2} \frac{1 - r_a}{1 - r_a \cdot a \cdot e^{i2k_\Omega L}}
\end{aligned} \tag{24}$$

where r_a is the reflection coefficient from the antenna end of the transmission line: $r_a = \frac{Z_a - Z_{TL}}{Z_a + Z_{TL}}$. Thus,

$$V_0^+ = \frac{V_a}{2} \cdot \frac{1 - r_a}{1 - r_a \cdot a \cdot e^{i2k_\Omega L}} = \frac{V_a}{2} \cdot t_a \tag{25}$$

where we introduced the transmission term (from the antenna to the transmission line) t_a . One can see that this formula contains the sum of an infinite geometric series corresponding to the multiple reflections from both ends of the transmission line. The result represents a cavity where one mirror is the circuit termination, and the other is the antenna-transmission line interface. Note that the $V_a, Z_a, Z_{TL}, \gamma, r$ parameters in the results presented further were simulated using the commercial software package CST Studio Suite. The simulated values of r are close to unity, meaning that the end of the transmission line can be approximately considered an open circuit termination. To better understand the physical meaning of the formula, let us consider two extreme cases for the transmission term.

1. Let $r_a = 1$. This would happen if $Z_a \gg Z_{TL}$. Then $V_0^+ = 0$, meaning that all the mmWave field was reflected at the "antenna - transmission line" interface, and no voltage entered the transmission line.

2. Let $Z_a = Z_{TL}$, thus $r_a = 0$ and the transmission line is matched to the antenna. Then $V_0^+ = \frac{V_a}{2}$.

Fig. 8 demonstrates r_a as a function of frequency for the dipole antenna and the transmission line used in this work.

The right-traveling mmWave electric field amplitude A_Ω might be found from the two forms of the expression for the right-traveling power of in the cavity $P_{mmW}^{on-chip}$:

$$P_{mmW}^{on-chip} = \frac{|V_0^+|^2}{2} Re \left(\frac{1}{Z_{TL}} \right) = \frac{1}{2} \varepsilon_0 n_\Omega c_0 |A_\Omega|^2 S_\Omega \tag{26}$$

Our simulations, together with the analytical model from [2] have shown the imaginary part of the characteristic impedance is negligible, so then $Re \left(\frac{1}{Z_{TL}} \right) \approx \frac{1}{Z_{TL}}$. This gives the relation between the amplitude of the mmWave field in the transmission line A_Ω and the incident mmWave electric field E_{inc} :

$$|A_\Omega| = IAF \cdot |t_a| \cdot \frac{1}{2\sqrt{Z_{TL}\varepsilon_0 n_\Omega c_0 S_\Omega}} E_{inc} \tag{27}$$

Finally, with this expression, one may introduce the side-band ratio (SBR) defined for a given input mmWave intensity

$$P_{SB+} = SBR \cdot P_p \tag{28}$$

where P_{SB+}, P_p are powers of the generated sideband and optical probe. Substituting eq. 27 into eq. 15 gives the following expression for the side-band ratio:

$$SBR = \frac{(\chi^{(2)} \cdot \omega_{SB+})^2}{4 \cdot n_o^2 \cdot n_\Omega \cdot c_0^3 \cdot \varepsilon_0 \cdot Z_{TL} \cdot S_\Omega} \cdot IAF^2 \cdot |t_a|^2 \cdot PM^2 \cdot E_{inc}^2 \cdot \Gamma_{eo}^2 \cdot L^2 \tag{29}$$

where we introduced the phase-matching function $PM = \left| \frac{e^{i\Delta\vec{k}L} - 1}{\Delta\vec{k}L} \right|$ describing the phase-matching of optical and mmWave modes, as well as the loss of the mmWave mode. By denoting $P_{mmW}^{on-chip} = \frac{IAF^2 \cdot |t_a|^2 E_{inc}^2}{2Z_{TL}} = \eta P_{mmW}^{free-space}$ we get:

$$SBR = \frac{(\chi^{(2)} \cdot \omega_o)^2 \cdot \Gamma_{eo}^2 \cdot L_{TL}^2 \cdot PM^2}{2 \cdot n_o^2 \cdot n_\Omega \cdot c_0^3 \cdot \varepsilon_0 \cdot S_\Omega} \cdot \eta P_{mmW}^{free-space} \tag{30}$$

where we introduced the coupling efficiency coefficient η of mmWave radiation from free-space to the transmission line and took into account that the probe frequency $\omega_o = \omega_p \approx \omega_{SB+}$, and $L = L_{TL}$.

3 Loss model

The analytical formulas for the various loss terms can be found in [2]. The main contributions to the loss are the conductor and radiative losses α_c and α_{rad} respectively. By introducing the frequency-dependent skin depth $\delta = \frac{1}{\sqrt{\sigma \cdot f_{mmW} \cdot \mu \cdot \pi}}$ and surface impedance $Z_S = \frac{1+i}{\sigma \delta} \coth\left((1+i)\frac{h_{Au}}{\delta}\right)$, the conductive losses are given by:

$$\alpha_c = g \cdot \operatorname{Re}\left(\frac{Z_s}{Z_{TL}}\right) dB/m \quad (31)$$

where the expression for the proportionality coefficient g is given by:

$$g = 17.34 \cdot \frac{P'}{\pi w} \cdot \left(1 + \frac{w}{w_{TL}}\right) \cdot \frac{\frac{1.25}{\pi} \ln\left(\frac{4\pi w_{TL}}{h_{Au}}\right) + 1 + \frac{1.25 h_{Au}}{\pi w_{TL}}}{\left(1 + \frac{2w_{TL}}{w} + \frac{1.25\pi h_{Au}}{\pi w} \cdot \left(1 + \ln\left(\frac{4\pi w_{TL}}{h_{Au}}\right)\right)\right)^2} \quad (32)$$

where w, w_{TL}, h_{Au} are the parameters as presented in section 1, and P' is:

$$P' = \begin{cases} \frac{k}{(1-\sqrt{1-k^2})(1-k^2)^{3/4}} \left(\frac{K(k)}{K'(k)}\right)^2, & \text{for } 0 \leq k \leq 0.707 \\ \frac{1}{(1-k)\sqrt{k}}, & \text{for } 0.707 \leq k \leq 1 \end{cases} \quad (33)$$

with $k = \frac{w}{w+2w_{TL}}$, $K(k)$ being a complete elliptic integral of the first kind, and $K'(k) = K(\sqrt{1-k^2})$. As shown in the same work, the radiative losses are proportional to the third power of frequency:

$$\alpha_{rad} = \pi^5 \frac{3-\sqrt{8}}{2} \frac{n_{\Omega}}{n_{sub}} \cdot \left(1 - \frac{n_{\Omega}^2}{n_{sub}^2}\right)^2 \cdot \frac{(w+2w_{TL})^2}{c_0^3 K'(k) K(k)} f_{mmW}^3 \quad (34)$$

where $n_{sub} \approx 3.41$ is the substrate's refractive index (silicon). Another contribution to the loss, a tangent loss α_t , can be simulated using, for example, CST Studio Software by simulating the 2D mode profile and relating the imaginary part of the effective refractive index κ_{Ω} as:

$$\alpha_t = \frac{4\pi \kappa_{\Omega} f_{mmW}}{c_0} \quad (35)$$

Combining all the above mentioned contributions of the loss we define the total loss $\alpha_{\Omega} = \alpha_c + \alpha_{rad} + \alpha_t$ and plot these various contributions in Fig.4. As it is clearly seen, the most dominant contribution comes from the conductor losses. One of the strategies on how to minimize this loss is to increase the metal thickness h_{Au} . We plot the losses for the various metal thicknesses h_{Au} in Fig.4. One may notice that the losses can be reduced significantly by increasing the metal thickness. The fabrication of the thicker electrodes might be challenging, however, it has been already demonstrated in [3].

4 Co- and counter-propagation mmWave radiation inside the transmission line

As it was described above, there are two waves propagating in the transmission line with the voltage amplitudes of V_0^+ and V_0^- , according to eq. 17. These voltage amplitudes correspond to the forward propagating electric field wave with an amplitude A_{Ω} and backward propagating wave A_{Ω}^- . In the case of the short transmission lines, whose length L_{TL} are comparable to the coherence lengths of the backward propagating wave $\left|\frac{\pi}{\Delta k_-}\right|$, the contribution of

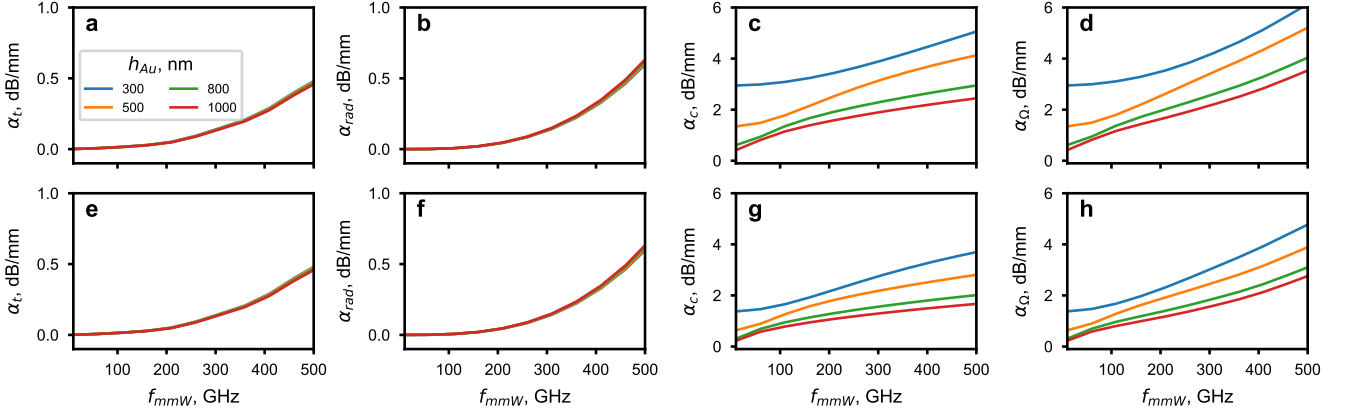


Fig. 4: Simulated loss for various electrode thicknesses and metal properties. (a, e) Tangent, (b, f) radiative, (c, g) conductor and (d, h) total loss versus mmWave frequency. Upper row: $\sigma = 1.91 \cdot 10^7$ S/m (as retrieved from the experimental data). Lower row: $\sigma = 4.1 \cdot 10^7$ S/m (literature value of gold conductance).

the second term in eq.14 is not negligible. Therefore, the electric field amplitude of the generated sideband A_{SB+}^{co} , when the optical probe co-propagates with the forward propagating mmWave mode, in accordance with eq.14 and 19 is proportional to:

$$A_{SB+}^{co} \propto A_{\Omega} \left(\frac{e^{i\Delta\tilde{k}_+ L_{TL}} - 1}{\Delta\tilde{k}_+ L_{TL}} + e^{i2k_{\Omega} L_{TL} - \alpha_{\Omega} L_{TL}} \frac{e^{i\Delta\tilde{k}_- L_{TL}} - 1}{\Delta\tilde{k}_- L_{TL}} \right) \quad (36)$$

If the optical probe is sent the other way around, so that it counter-propagates the forward propagating mmWave mode, then its amplitude will be given by

$$A_{SB+}^{counter} \propto A_{\Omega} \left(\frac{e^{-i\Delta\tilde{k}_- L_{TL}} - 1}{\Delta\tilde{k}_- L_{TL}} + e^{i2k_{\Omega} L_{TL} - \alpha_{\Omega} L_{TL}} \frac{e^{-i\Delta\tilde{k}_+ L_{TL}} - 1}{\Delta\tilde{k}_+ L_{TL}} \right) \quad (37)$$

as now the phase-matching conditions will be the opposite for the forward- and backward-propagating mmWave waves. Now, by introducing the difference sideband ratio $dSBR = 10 \cdot \log_{10} \left(\frac{|A_{SB+}^{co}|^2}{|A_{SB+}^{counter}|^2} \right)$, we get:

$$dSBR = 20 \cdot \log_{10} \left(\frac{\left| \frac{e^{i\Delta\tilde{k}_+ L_{TL}} - 1}{\Delta\tilde{k}_+ L_{TL}} + e^{i2k_{\Omega} L_{TL} - \alpha_{\Omega} L_{TL}} \cdot \frac{e^{i\Delta\tilde{k}_- L_{TL}} - 1}{\Delta\tilde{k}_- L_{TL}} \right|^2}{\left| \frac{e^{-i\Delta\tilde{k}_- L_{TL}} - 1}{\Delta\tilde{k}_- L_{TL}} + e^{i2k_{\Omega} L_{TL} - \alpha_{\Omega} L_{TL}} \cdot \frac{e^{-i\Delta\tilde{k}_+ L_{TL}} - 1}{\Delta\tilde{k}_+ L_{TL}} \right|^2} \right) \quad (38)$$

5 Measurements of the antenna-transmission line reflection coefficient

We performed the measurements of the sideband ratio, shown in Fig.6 of four devices with various lengths: 0.25, 0.5, 1 and 2 mm. Since each time we place the silicon lens on the back of the chip, there might be a slight displacement of the antenna with respect to the center of the silicon lens, for each set of measurements, we calculated the coupling efficiency. As a reference, we used the device with a 2 mm transmission line length. The results for this experiment are shown in Fig. 5, together with the linear fit of the coupling efficiency, which will be used later below.

Then, we performed the measurements of the three left devices with the transmission line lengths 0.25, 0.5 and 1 mm and the results are shown in the Fig.6a-c.

The fitted value of the $r_a^{fit} = 0.653e^{-i \cdot 0.085\pi}$ is very close to the simulated one plotted in Fig.3 of the main text both in amplitude and in phase. Another interesting finding is the dependence of on- and off-resonant SBR per $P_{mmW}^{free-space}$ as a function of the transmission line's length. We noted that it scales as L_{TL} for the on-resonance case,

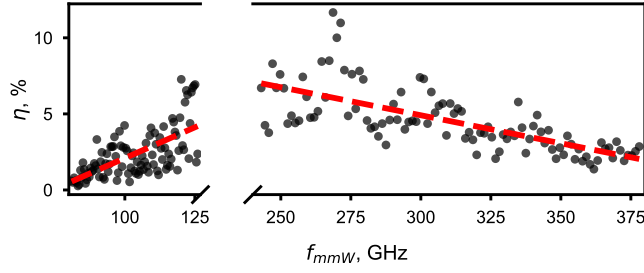


Fig. 5: Coupling efficiency of the mmWave free-space radiation to the chip performed right before the reflection coefficient measurements at the antenna-transmission line interface.

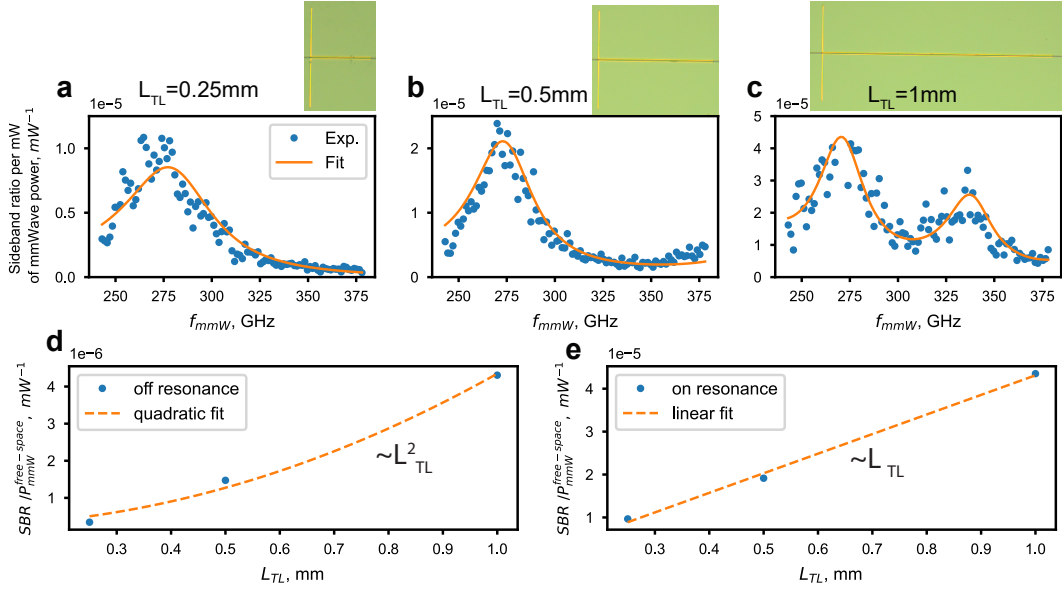


Fig. 6: The sideband ratio per $P_{mmW}^{free-space}$ as a function of mmWave frequency and the device photograph with the length of transmission line (a) 0.25 mm; (b) 0.5 mm; (c) 1 mm. The dependence of (d) off-resonance (min value across the whole frequency range) and (e) on-resonance (the mean value in the range 270-280 GHz) sideband ratio per $P_{mmW}^{free-space}$ as a function of the transmission line length. Dashed lines indicate the fits.

while as L_{TL}^2 for the off-resonance case in good agreement with eq.29. This may indicate that in on-resonance case, the field enhancement coming from the term $\frac{1}{|1-r_a \cdot a \cdot e^{i2k\Omega L}|^2}$ compensates for the shorter interaction lengths.

Then, we performed the same measurements across WR9.0 band, and plotted the results in Fig.3 of the main text. The fitted value of the $r_a^{fit} = 0.729e^{i \cdot 0.464\pi}$ is again very close to the simulated one plotted Fig.3 of the main text.

We used the CST Studio software to simulate the impedances of the antenna and the transmission line. These values are shown in Fig.8

6 Linewidth of the optical microring resonance

We performed the transmission measurement of the ring resonator in order to get the linewidth of the pumped resonance. We plot the transmission spectrum of the resonance we pumped for the experiments in the electro-optic comb generation in Fig.9 as well with the statistics over multiple resonances. We pumped the resonance with the linewidth of ≈ 220 MHz and this value was further used in the calculations.

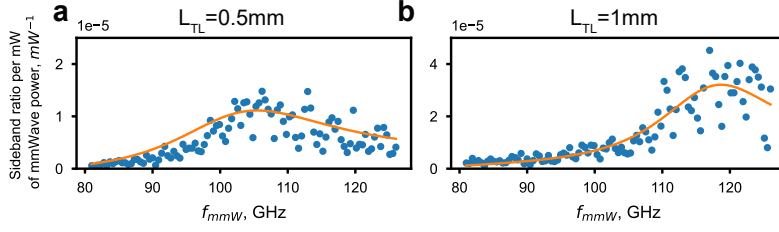


Fig. 7: The sideband ratio per $P_{mmW}^{free-space}$ as a function of mmWave frequency and the device photograph with the length of transmission line (a) 0.5 mm; (b) 1 mm.

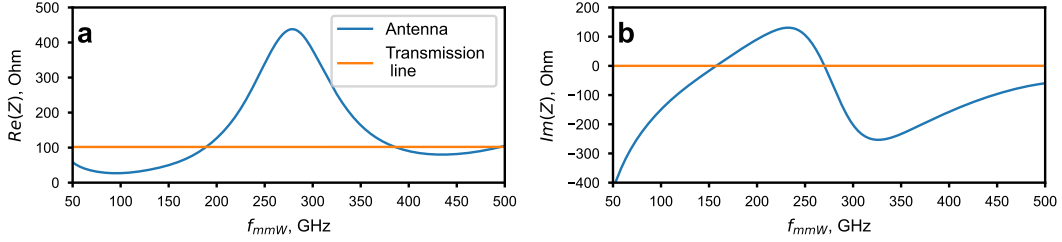


Fig. 8: The simulated real (a) and imaginary parts (b) of the antenna and transmission line impedance.

7 Measurements of the coupling efficiency for the experiment with the ring resonators

As described above, we measured the coupling efficiency each day prior to conducting the main experiments. For these measurements, we used a test device consisting of a 2mm-long transmission line with a dipole antenna. The measured coupling efficiencies are presented below in Fig.10.

We note the coupling efficiency at frequencies below 125 GHz because the TPX lens could not be used due to the setup's constraints and the limited space behind the chip.

8 Strategies on improving the coupling efficiency of the mmWave radiation to the chip

As discussed above, the coupling efficiency depends mainly on two parameters: IAF and r_a . Then, IAF might be optimized in two different ways: by optimizing the parameters of the free-space gaussian mmWave beam (such as the beam waist) illuminating the chip by developing the lens system, or by engineering the design of the antenna and using other types of antennas, such as bow-tie [4], bull eye [5], LC [6] and others. In addition, the reflection coefficient at the antenna-transmission line r_a significantly affects the coupling efficiency. Broad- or narrowband coupling efficiency optimization is considered depending on the application. In the first case, the r_a must be minimized across the entire frequency range of interest, bringing the values of $t_a = \frac{1-r_a}{1-r_a \cdot a \cdot e^{i2k_\Omega L}}$ to 1. However, in the case of narrowband optimization, one may consider exploiting the resonant behavior of the term t_a as $r_a \rightarrow -1$. By minimizing the round-trip propagation loss a , one may benefit from the enhancement of the intra-cavity field at frequency where $\arg(r_a \cdot e^{i2k_\Omega L}) = 2\pi m$ with m being an integer number. We demonstrate the possibility of engineering the r_a coefficient to be significantly low across a large frequency range by simulating the reflection coefficient of the bow-tie

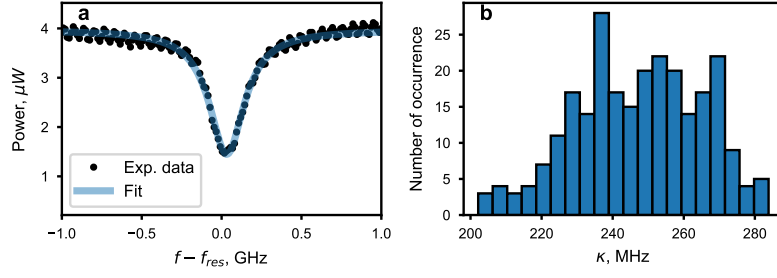


Fig. 9: (a) The transmission spectrum of the pumped resonance and (b) linewidth statistics over 256 resonances

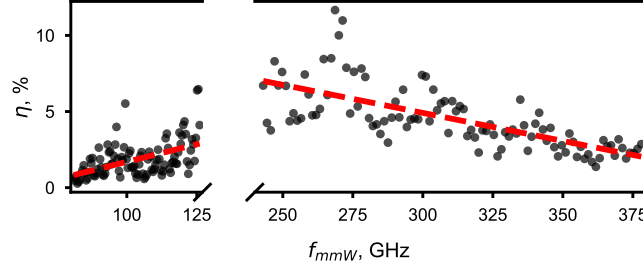


Fig. 10: Coupling efficiency of the mmWave free-space radiation to the chip performed right before electro-optic comb measurements.

antenna with a width of 300 μm and a height of 400 μm , as presented in the Fig. 11.

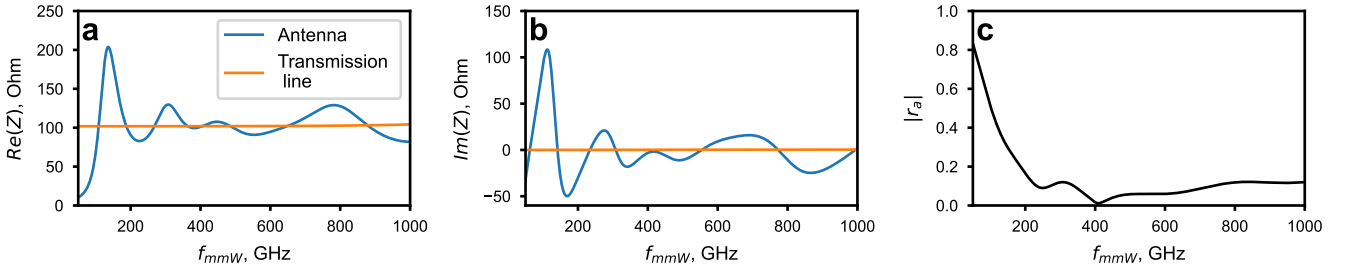


Fig. 11: Simulation results for the bow-tie antenna. (a) Real part of the impedance; (b) Imaginary part of the impedance; (c) reflection coefficient between the bow-tie antenna and the transmission line demonstrating flat and low reflection coefficient r_a across frequency range of 200-1000 GHz.

References

- [1] D. M. Pozar. Microwave engineering; 3rd ed. Wiley, Hoboken, NJ (2005).
- [2] U. D. Keil, D. R. Dykaar, A. Levi, R. F. Kopf, L. Pfeiffer, S. B. Darack, and K. West. “High-speed coplanar transmission lines.” *IEEE journal of quantum electronics*, **28**(10):2333–2342 (1992).
- [3] C. Wang, D. Fang, J. Zhang, A. Kotz, G. Lihachev, M. Churaev, Z. Li, A. Schwarzenberger, X. Ou, C. Koos, et al. “Ultrabroadband thin-film lithium tantalate modulator for high-speed communications.” *Optica*, **11**(12):1614–1620 (2024).

- [4] I.-C. Benea-Chelms, T. Zhu, F. F. Settembrini, C. Bonzon, E. Mavrona, D. L. Elder, W. Heni, J. Leuthold, L. R. Dalton, and J. Faist. “Three-dimensional phase modulator at telecom wavelength acting as a terahertz detector with an electro-optic bandwidth of 1.25 terahertz.” *Acs Photonics*, **5**(4):1398–1403 (2018).
- [5] M. Beruete, U. Beaskoetxea, M. Zehar, A. Agrawal, S. Liu, K. Blary, A. Chahadih, X.-L. Han, M. Navarro-Cía, D. Etayo Salinas, A. Nahata, T. Akalin, and M. Sorolla Ayza. “Terahertz Corrugated and Bull’s-Eye Antennas.” *IEEE Transactions on Terahertz Science and Technology*, **3**(6):740–747 (2013).
- [6] Y. Salamin, I.-C. Benea-Chelms, Y. Fedoryshyn, W. Heni, D. L. Elder, L. R. Dalton, J. Faist, and J. Leuthold. “Compact and ultra-efficient broadband plasmonic terahertz field detector.” *Nature communications*, **10**(1):5550 (2019).